STARS

Electronic Theses and Dissertations, 2020-

2020

Experimentation and Simulation of Pulsed Eddy Current Thermography of Subsurface Aircraft Corrosive Defects

Johnathan Hernandez
University of Central Florida

STARS Citation

University of Central Florida

Showcase of Text, Archives, Research & Scholarship

EXPERIMENTATION AND SIMULATION OF PULSED EDDY CURRENT
THERMOGRAPHY OF SUBSURFACE AIRCRAFT CORROSIVE DEFECTS

by

JOHNATHAN HERNANDEZ
B.S. University of Central Florida, 2018

A thesis submitted in partial fulfilment of the requirements
for the degree of Master of Science
in the Department of Mechanical and Aerospace Engineering
in the College of Engineering and Computer Science
at the University of Central Florida
Orlando, Florida

Spring Term
2020

Major Professor: Seetha Raghavan

ABSTRACT

During the life cycle of aircraft, external structures are under constant attack from environmental degradation in the form of corrosion. Corrosive defects consist of multiple types of surface and subsurface damage that are often undetectable due to surface coatings or insulation leading to loss in structural integrity. Non-destructive techniques for corrosion detection typically require the removal of paint. Detection of corrosion under insulation (CUI) is highly valuable for cost and time effectiveness. Although techniques have been developed for detection of CUI, not many of these satisfy the criteria for portability and hangar operation. To address this, multiple techniques were investigated yielding Pulsed Eddy Current Thermography (PECT) as a promising technique to pursue a proof of concept. Through multiphysics simulation using COMSOL, case studies were developed to understand and predict the temperature responses of aircraft materials when altering the current, lift off, and defect size and to design the coil for optimal non-destructive detection capabilities. Initial studies were conducted on various samples including coated and uncoated Aluminum, Carbon steel, Zinc-galvanized carbon steel with different types of corrosion. A novel in-house MATLAB© code was developed for post-processing of the corroded samples. Initially, defect localizations through edge heating or from dissipation were captured through IR thermography. To address issues with non-uniformity of heating that decrease the accuracy and precision of this technique, the thermal change with respect to time was analyzed through each frame and decomposed using Fourier transform from the time domain to a frequency domain. Manufactured corroded defects made through salt fog and acid baths, such as pitting voids, were detected under insulation of 125 microns with diameters ranging from 0.5 - 1 mm for all material systems. These results show the high potential of PECT for aerospace on-field applications providing location and shape for defects under insulation.

This work and any work I will ever do is dedicated to you, Mom. There is no one on this planet that truly has blessed me in my life more than my mother, I am who I am today because she filled in the shoes of every role. Thank you, Mom

"Wanted my family to come to my games, My mama couldn't make it 'cause she was at work, Lived with my grandma, she took me to church" –Meek Mill

"Part of me had to die so a part of me gets to live, I thank the Lord 'cause I don't look like what I been through" –Ace Hood

"I feel like it's just me. Look, I feel like I can't breathe. Look, I feel like I can't sleep. Look, I feel heartless, often off this Feelin' of fallin', of fallin' apart with Darkest hours, lost it" –Kendrick Lamar

"If you weigh me down then I gotta remove you, If you in my way, then I gotta go through you" –Big Sean

ACKNOWLEDGMENTS

TABLE OF CONTENTS

LIST OF FIGURES

LIST OF TABLES

CHAPTER 1: INTRODUCTION

During the life cycle of many aircraft, the structural integrity is degraded by the presence of corrosive mechanisms formed in a high moisture environment. Corrosion is an electrochemical reaction in which a refined metal will become more chemically stable. This reaction will then cause the material to become acidic in nature, resulting in a material loss [21]. There are two major types of corrosion: galvanic and direct chemical attack. Galvanic corrosion, in aircraft particularly, is common and results in multiple types of corrosion "defects" forming during the life cycle [21, 22, 23]. These corrosion reactions lead to major crack propagation resulting in possible mechanical failure modes. Corrosion-based defects and cracks are not only one of the most frequent but also one of the costliest types of degradation modes due to loss in flight hours from inspection and maintenance. This loss of flight hours can result in a financial loss of around 6 billion US dollars in the DoD for aircraft alone [24, 25, 19, 26]. Annually, corrosion damage is only noticed and managed retroactively, after it has been identified by visual inspection through a time-intensive process looking specifically for bubbling, blistering, and flaking [19]. Unfortunately, along the life cycle of these aircraft multiple types of corrosion can degrade the structure; this degradation can lead to cracks due to loss of load carrying capacity and ultimately leads to failures of structural systems [27]. As a result, corrosion is one of the largest cost drivers for the DoD, as is shown in Table 1 where availability is given in terms of hours the aircraft is out of service, and where the acronym "NAH" refers to non-available hours. To prevent the rise of these costs, a reliable and accurate characterization of corrosion damage and tracking is needed before critical damage is visually observed.

Table 1.1: Table Estimated cost of corrosion in the DoD for aerospace structures [19]

Study Segment	Corrosion cost impact			Corrosion availability impact		
	Maintenance cost ($ millions)	Corrosion cost ($ millions)	Corrosion percentage	Total NAHs	Corrosion NAHs	Corrosion percentage
Aviation and missiles	24,501	5,669	23.6	15,247,874	2,151,683	14.1
Other equipment	1,661	237	14.3	-	-	0
Total	25,712	5906	23.0	15,247,874	2,151,683	14.1

1.1 Corrosion of Aircraft Structures

In the Aircraft industry, structural integrity of components is paramount in order to ensure high factors of safety. Bearing structures made of aluminum alloy and other metals are designed to maintain the external and internal aircraft loads during flight, take off, and landing. During the lifetime of an aircraft, defects from stress concentration or corrosion can result in major degradation throughout the life cycle of individual aircraft parts and systems.

1.1.1 Corrosion Mechanics

Corrosion is a natural chemical change of a material in which it reverts from being a refined metal to a more chemically stable state [22, 28, 29]. This chemical reaction is dependent on environmental and material factors and is controlled by kinetic and thermodynamic process. Corrosion involves an increase in the oxidation state of metallic atoms, thus liberating electrons. The consumption of these liberated electrons is done through reduction, often due to acidic hydrogen environments. Atoms that lose an electron are deemed anodes, while those that receive electrons are referred to as cathodes. Between these elements, a current transmits the electrons that are generated due to the potential difference (V) [30, 31, 32]. This is shown in Figure 1.1, where localized pitting corrosion demonstrates the corrosion theory. Direct chemical attack corrosion is due to the

immediate presence of an acidic system, like battery acid on the metal plates in the electrical bay in an aircraft structures [21, 29, 22]. However, in an aircraft's life cycle the exterior will be subjected to galvanic corrosion. Multiple corrosion types found on aircraft will be explained in further detail in the following sections.
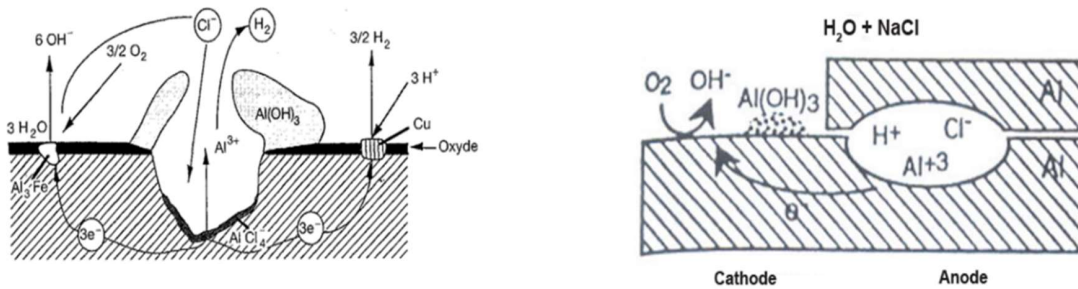
Figure 1.1: Corrosion mechanics of typical galvanic corrosion demonstrating the transfer of electrons between cathode and anode.[1]

1.1.2   Types of Corrosion

Galvanic corrosion occurs when two electrochemically dissimilar metals with a potential difference are put together in the presence of an electrolyte (or a corrosive environment). The electropotential difference between the anode and cathode drives the kinetic of corrosion. In this process, the anode is dissolved and undergoes a loss of material. Corrosion, being a reaction, leads to products that add attributes and cause visual and non-visual changes seen in the material such as pitting, flaking, blistering, and cracks [28, 22, 29, 1].

Pitting corrosion or general corrosion is a localized form of surface corrosion causing voids with trapped corrosion agents[30]. These corrosion agents, anions such as chloride, can infiltrate a

material film. Anions can affect metals such as aluminum even though it creates an oxidation barrier of aluminum oxide, which protects against corrosion in locations where there are local defects and places of a weakened film. This interaction can result in the creation of a pit within the material; this pit becomes an electrolytic cell containing corrosion agents, trapped moisture, and acidification which increases the rate of corrosion within the pit. On the boundary of the pit, the same solution solidifies into a pit cover, due to neutral charge or lack of water, disincentivizing the corrosion process[30, 33]. This pit, the formation of the pit, and its cover appears to be problematic due to the difficulty of detection it poses, and this system becomes a spot of stress concentration.

Crevice corrosion is another form of localized corrosion which occurs in environments where there is poor oxygen circulation like crevices in rivets, screws, and joints. This macroscopic environment traps moisture and corrosion products, accelerating the corrosion rate [34]. The mechanism and reactions that take place are the same as the ones that are driving pitting corrosion; however, crevice corrosion does not create defects in the same manner as pits in the thin film, but takes place in the macroscopic environment based on the geometry of the substrate of focus [35].
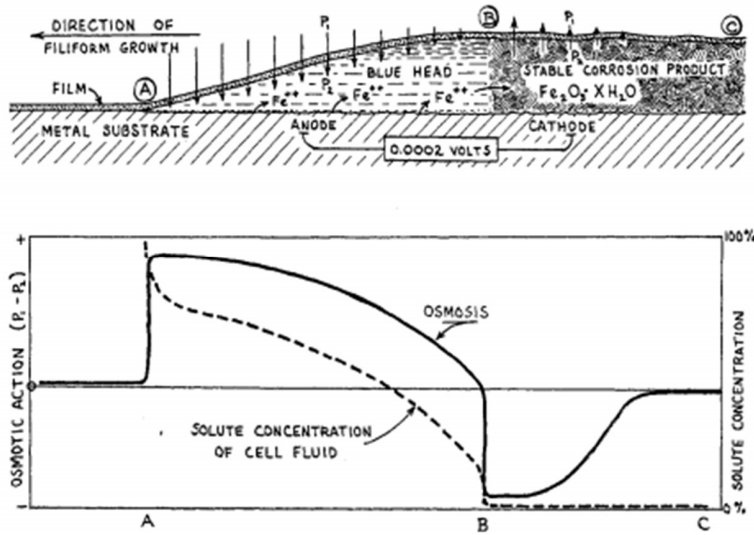
Figure 1.2: Filiform corrosion and products from rust [2, 3]

Filiform corrosion, or under film corrosion, is the formation of threadlike filament of corrosion products beneath an organic film such as paint. This corrosion process stems from corrosion agents penetrating the organic film in places where there are weak points or discontinuities. It has been recorded that the growing head of the filament is anodic to the metallic substrate, meaning that galvanic corrosion occurs as the developed filament is left with stable corrosion products, as shown in Figure 1.2. The solute concentration of cell fluid results from water infiltrating through osmosis or capillary action. As the solute is introduced between the organic film and metallic substrate, osmosis takes place and achieves equilibrium. In addition, oxidation occurs and creates the corrosion products. The corrosion products that are introduced create a pressure difference in which the vapor pressure is greater than atmospheric, allowing it to expand to achieve equilibrium. The filament achieves its equilibrium at a certain point, the remaining solute is displaced further away to a connecting region allowing it to continue to oxidize [2, 35].

5

Figure 1.3: Cracks branching inter-granular in stress corrosion cracking [2, 3].

Intergranular corrosion, shown in Figure 1.3, is a type of corrosion that occurs due to the imperfect machining and damages from initial assembly of the component. The non-uniformity in the manufacturing process can result in irregular open grains, or microscopic ditches in its surface, which can be penetrated by corrosion agents; this allows for the same mechanisms of pitting corrosion to take place inside the open grains as it contains a similar environment as the acidification in that area increases. This will lead to exfoliating of the grains and propagation of cracks, which are difficult to detect, as the degradation process stems from micro cracks of the material before severe damage occurs [2, 3, 36].

Fretting corrosion is the result of fretting on structural bolted joints. Fretting will cause joints to wear down through friction, creating a dark powder or paste as a by-product. The surfaces and edges where by-product has been created will have cracks which may develop across the component. These cracks will create an environment in which pitting corrosion can take place [2, 3, 36]. Exfoliation corrosion develops from the unprotected or damaged areas of metals where grains may be exposed to the environment, allowing for corrosive agents to enter. This corrosion is commonly characterized as a loss of material or an increase of roughness in the surface, which

may be delamination [36]. Lastly, stress corrosion cracking is a corrosive defect that occurs due to the combination of the acidic environment in a area with moving parts under load. These bearing structures will begin forming voids and pits that will result in stress concentration areas. Pits will then begin to propagate in an accelerated manner due the stress on the aircraft structure [2, 28].

Many of these types of corrosion can be found on various aircraft structures and sub-systems over time when exposed to corrosive environments. Methods to detect signs of corrosion on a aircraft are critical for structural integrity. Non-destructive and non-contact detection techniques are especially useful for early detection and have potential for on-field ease of use.

1.2 Current State of the Art for Corrosion Detection

Several new and existing techniques have shown potential for corrosion detection including: Hyperspectral Imaging (HSI), Terahertz (THz), Eddy Current (EC), Infrared Thermography (IRT), Microwave Imaging (MI), Pulsed Eddy Current Thermography (PECT), Electrochemical Methods (ECM), Radio Frequency Identification (RFID), Ultrasonic Waves (UW), Compton Backscattering (CBS), and Acoustic Emission (AE). All these techniques are considered to be non-destructive techniques, but most of these techniques are often restricted to "in-lab" studies. Advantages, limitations, and positive outcomes of these techniques have been assessed and described here below.

1.2.1 Hyperspectral Imaging

A popular and emerging technique in the aerospace industry is hyperspectral imaging. Typically used for medical and agriculture applications, hyperspectral imaging utilizes the ability of taking "snap shot" scenes and highlighting regions of the image where the material is localized. This ability that hyperspectral imaging uses, is the concept of "data cubes" as a 3D representation of

7

pixels collected by the reflection of the excited material as a function of wavelength. This reflection can be emitted from the molecular structure of the material via passive light like sunlight or active light from an artificial light source. This cube of data is based off of reflection and has a spatial x and y axis and a continuous spectral z axis which is shown in the conceptual Figure 1.4 [4, 37, 38].
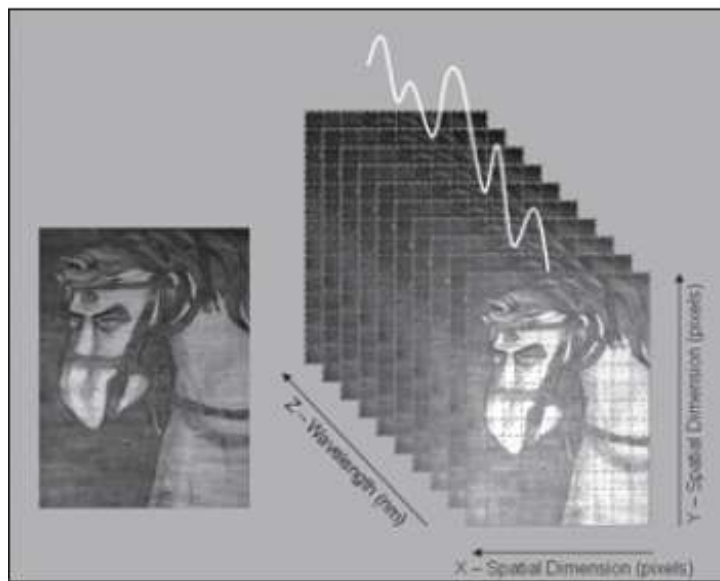
Figure 1.4: Hyperspectral cube built through spectral bands [4].

This spectral response is unique to a material's molecular structure, which allows material identification or emission response. Corrosion detection using this technique looks at the reflective loss in a material due to the degradation. Currently, work to make handheld systems for medical applications has shown positive outcomes. However, for corrosion detection, limitations in data analysis time and reflectivity of corrosion products has shown the need for more work before industrial implementation [4, 37, 38, 39, 40]. This issue with spectra detection of corrosion related damage, is one of the disadvantages of hyperspectral imaging used in this application. Another disadvan-

tage of hyperspectral imaging is related to the reflection data itself. Variable lighting can affect the spectrum since the reflectivity is directly correlated to the amount of excitation the material is receiving. Besides variable lighting, illumination of these materials needs to be filtered out with processing to collect the reflectivity spectrum. Even without the illumination, the post-processing for these scenes can be time-consuming due to the large amount of data collected for each of these hyperspectral cubes. Each of these cubes, which only represents one pixel, can have a large range of wavelengths with there being hundreds of thousands of pixels per scene [4, 37, 40].

1.2.2   TeraHertz Imaging

Terahertz (THz) has been used extensively for defect characterization, including corrosion, in laboratory applications. THz radiation can characterize defects by measuring surface roughness and the paint's film thickness. THz technology is based on using a femto-second electromagnetic source to excite material in the frequency ranges of 100 GHz to 10 THz with resolution as low as the sub-micron level, i.e. 0.8 μm, depending on equipment [5, 41, 42]. THz radiation, such as that produced by microwaves, can penetrate material and reflect when it interfaces with defects like voids and inclusions. Since THz can be pulsed, these discontinuous responses can be easily translated into time-domain signals like ultrasonics, where change in mode or phase is unique to material properties or interferences. THz can also generate absorption spectroscopy from transmission signal instead of reflectivity. This absorption spectra also behaves as a spectral "fingerprint", which is unique to a material's molecular structure. The ability of THz technology to use multiple methods to characterize materials makes it a very strong technology in non-destructive evaluation (NDE) for corrosion studies. Most results of THz can be post-processed into "images" to highlight specific results. These images are generated by taking point by point raster scans that are superimposed into one image. For example, the different response of reflective amplitude of the signal in time domain THz(TD-THz), shown in Figure 1.5 below, displays how higher amplitudes from the

9

post-processed images relate to the paint thickness [5, 41, 42, 43].
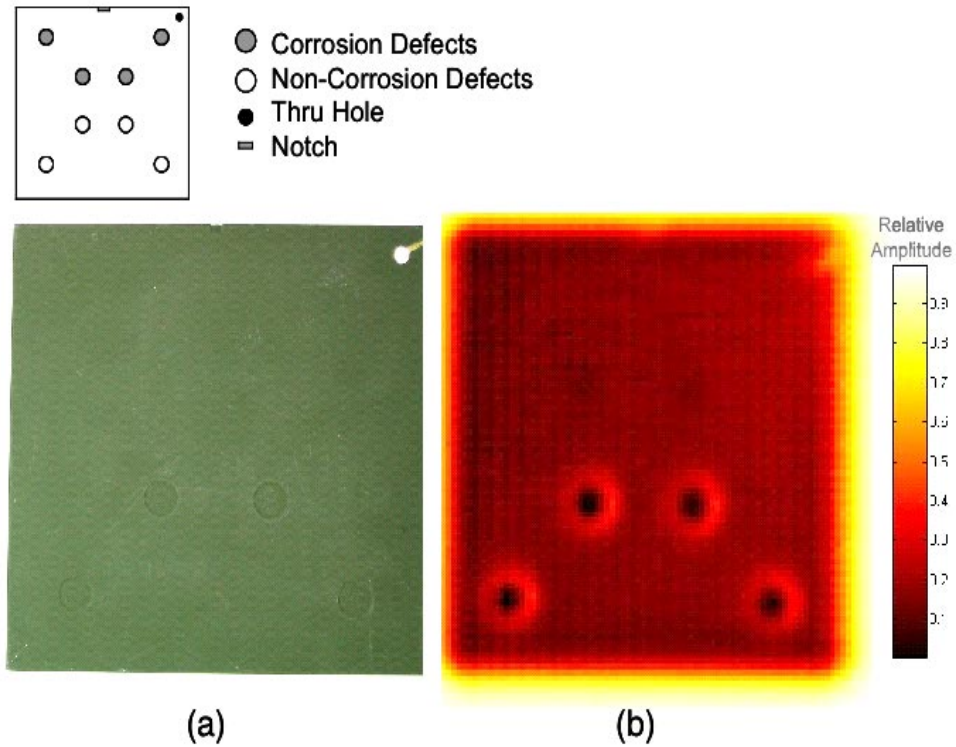
Figure 1.5: Paint thickness and delamination measured through THz spectroscopy [5].

1.2.3 Eddy Current Imaging

Eddy current technology is an older technique that has been used commonly in the industry as a non-destructive method for evaluating damage and defects on conductive material [6]. The methodology uses electromagnetic fields to characterize any damage or defects on the material. Most eddy current setups include a material that is an electrical conductor in the shape of a coil. This involves the use of an alternating current to run into the coil, at a chosen frequency, to develop a magnetic field expanding and collapsing into the coil. When the coil's magnetic field

encompasses a conductive material, electromagnetic induction will occur and produce eddy currents. The eddy currents in the material begin to induce their own magnetic field that collides with the original field from the coil [44]. When the magnetic field of the coil comes across a defect like a crack or void, the magnetic field is disrupted, changing impedance. The frequency chosen for eddy current can be anywhere from 100 Hz to MHz for single frequency types [6, 44].
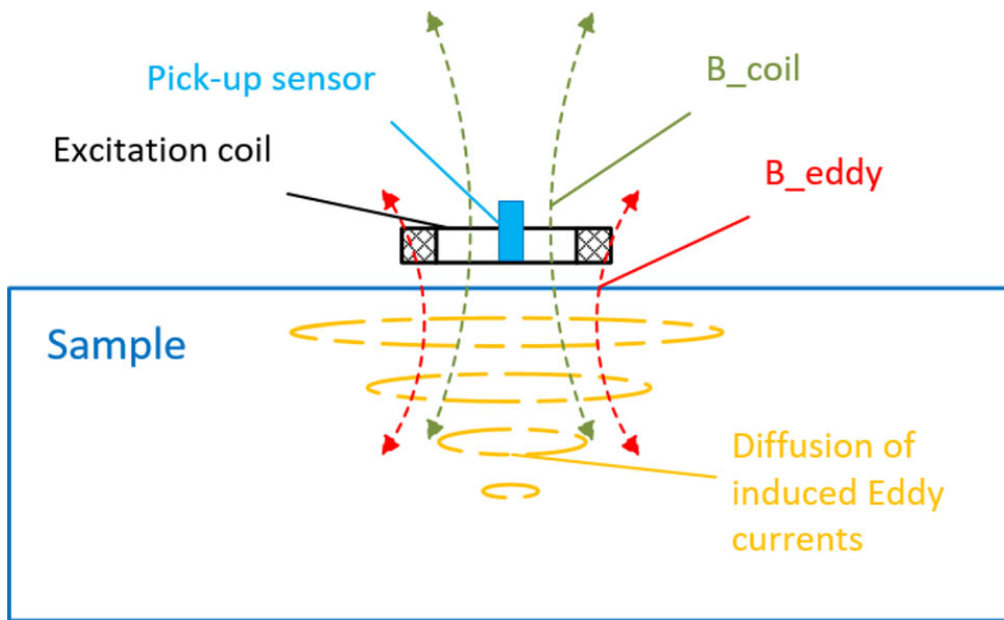
Figure 1.6: Methodology of Eddy current methods for material characterization [6].

Typical eddy current instruments characterize defects using this method with single frequency. Eddy currents, however, are not only limited to defect detection but can also do material identification, material thickness, coating thickness, and more. Since the physics behind this non-destructive technique is electromagnetic, conductivity and magnetic permeability of the material in question, eddy current imaging can also be used to characterize any changes to the material due to heat changes, as the conductivity will be altered. Eddy current techniques are actively used in the

11

industry for crack and void detection typically when the defect is generally known. This measurement can be improved through higher pulses or modulated pulsating of these magnetic fields. This technique has been industrialized for quite some time, and is one of the few techniques with large impact in the NDE industry. A disadvantage that can be listed for this technique is the high cost of magnetic sensors. There is a need for machine learning and defect libraries to be developed [44, 45, 46, 47, 48, 49].

1.2.4 Infrared Thermography

Infrared thermography is another industrialized solution that has been adapted to detect defects and corrosion. Spatially resolved thermography uses radiation due to a change in temperature to characterize defects. As thermal propagation occurs in a material, if there are no defects, a uniform thermal response will propagate into the system. However, if there are defects, contrast localizations will occur around the edge during heat generation and under the defect during cooling. Multiple applications of infrared thermography in passive and active thermography have been used in the industry for many years now [50, 51, 52, 53, 54, 55]. Systems like PECT, flash thermography, and passive structural health thermography all fall within this category. Passive IRT is used extensively in condition monitoring of equipment and structures to ensure integrity. Passive IRT is focused more on the system of interest's self-emission to monitor any extreme temperature changes [56, 57, 41]. In active IRT, another system excites the sample of interest to stimulate the material with a heat flux. Treating the heat flux as a 1D transient wave through the material, the Infrared (IR) camera will collect all the thermal changes within the material. As the uniform temperature rises along the sample, a localized high temperature will occur over any defects in the material due to insulation effects of the defect. These localized areas can then be used to outline the shape of the defect, making IRT a powerful system for locating and characterizing defects in materials. There are three major types of active thermography: pulsed, locked in, and pulsed phase

(a mixture of locked and pulsed). Each of these types of thermography uses the 1D transient heat flux model to characterize defects; however, the application of heat flux to the specimen is quite different with advantages and disadvantages for each type [56, 58]. To increase accuracy and resolution for corrosion and defect detection, Maldague et al. extended this temperature measurement to phase analysis, which improved the capabilities of active infrared techniques [52, 53]. Limitations of this technique are related to the active system used, coil, lamp, or laser, which can cause non-uniform heating and the requirement of an expensive camera system.

1.2.5 Microwave Imaging

Microwave technology has been used for non-destructive testing since the 1990s. Microwave spectrum frequency range is from 30-300 GHz and wavelength range is from 10 to 1 mm [20]. These microwave NDE methods are useful for penetrating inside dielectric materials without high attenuation. As the excitation source interacts with the material, it reflects or diffracts these microwaves which are used to study changes in phase and amplitude of these reflected waves [7]. For most experimental testing, several bands of interest in the microwave spectrum are used to compare the difference in phase and amplitude change along each of those bands, as shown in Table 1.2. 1.2

Table 1.2: Frequency chosen to detect dielectric properties of corroded produced Al_2O_3 [7, 20]

| | | Average Values for Real Al_2O_3 | | |
| | | | Standard Deviation | |
Frequency (GHz)		Dielectric Constants	Real	Imag.
S-Band	2.6-3.95	N/A	N/A	N/A
G-Band	3.95-5.85	4.036-j0.430	± 0.023	± 0.015
J-Band	5.85-8.2	3.337-j0.285	± 0.033	± 0.013
X-Band	8.2-12.4	3.495-j0.357	± 0.023	± 0.011
Ku-Band	12.4-18.0	3.83-j0.373	± 0.029	± 0.007

The uniqueness of this method is its ability to use the dielectric properties of materials to compare materials. For corrosion detection, there are advances and restrictions that apply depending on the material of interest. However, unlike electromagnetic NDEs, microwave is not limited to only conductive materials. The studies done by Hughes et al. with different aluminum panels produced strong results of detection in alumina oxide, paint, and aluminum itself [59]. Unfortunately, the characteristics of the dielectric parameter did not have enough variance to conclude that the damage was due to corrosion. Methods to improve this issue include the implementation of a defect library to characterize different defects. Microwave experiments are shorter in time compared to point by point measurements due to the probe set up, but testing can still be lengthy due to the possibility of selecting multiple bands. Research has been done to limit the corrosion characterizing test time by limiting the number of bands to a K band (18 - 26.5 GHz) sweep along the scan across the sample. With this sweep, an average magnitude across this frequency is used to process the images. In this study, the sample was coated steel where the permittivity could be calculated and compared to the

permittivity of iron oxides and hydroxides like Fe_2O_3 [7, 59, 60, 61, 62]. This microwave imaging is shown in Figure 1.7.
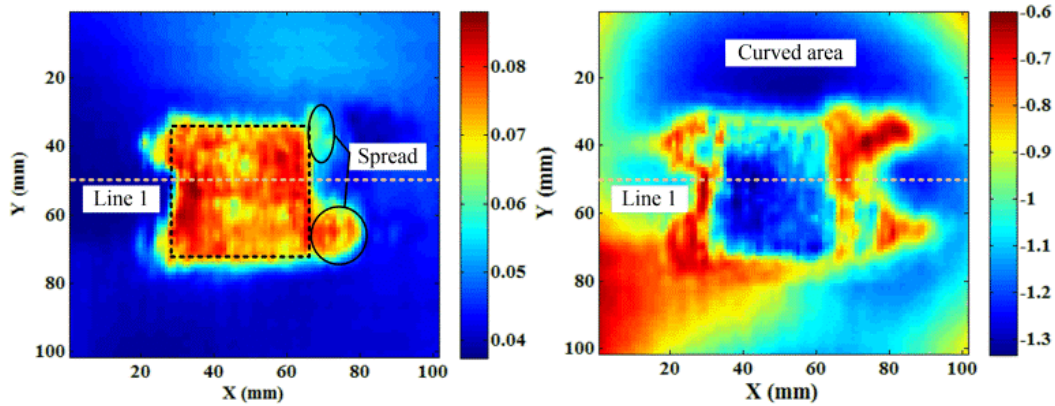
Figure 1.7: Microwave imaging of corrosion on steel panel with single paint layer [7].

1.2.6   Electrochemical Methods

Electrochemical corrosion detection NDTs include and are not limited to electrochemical impedance spectroscopy (EIS) and electrochemical noise measurement (ENM). Unlike other methods, this methodology measures the change of resistor impedance along the painted film. Electrochemical methods much like magnetic flux leakage (MFL) are used actively in industry for real time monitoring of piping systems and nuclear plants. Typically, EM methods are in contact with the surface under inspection by a cell and sensors. A typical setup consists of a counter electrode, a reference electrode, a working electrode sensor, the coated sample, and electrolyte gel in need that sits in between the cell and the substrate material. These cells are connected to a potentiostat, which applies a voltage to generate a current throughout all in contact systems. The reference electrode and counter electrode are in a cell filled with the electrolyte gel (which solution tries to mimic the environment). The working electrodes, outside the cell, will measure the voltage through the material

15

system. The electrolyte gel will penetrate the film coating via microstructure defects or porosities that come in contact with the substrate [8, 63, 64, 65, 66, 67]. An example of this electrochemical setup can be seen in Figure 1.8.
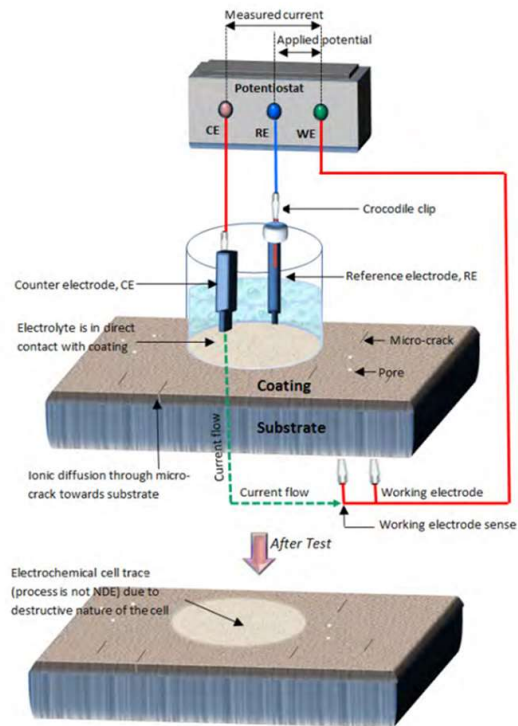
Figure 1.8: Electrochemical cell method for corrrostion detection [8].

The voltage collected from the potentiostat will be converted into an impedance spectrum based on an equivalent circuit in reference to the sample of interest. Based off these circuits, dependent on the material under investigation, equations will be modeled to obtain the impedance spectrum [8, 64, 67, 66]. These spectra will be compared to a reference spectrum collected on non-corroded or damaged surface. While the current is running through the system, impedance will change as different cracks or defects act as resisters being added to the circuit changing the voltage,

16

impedance, and current. These changes can be tracked to determine localization of defects on the specimen by moving the cell to different locations. A disadvantage with this is that after removal of these cells, the solution can damage the coating, requiring recoating. In an effort to increase and reduce portability, permanent magnets have been implemented on the cell so the cells can be attached to multiple surfaces. The issue is that the magnetic field emitting from these magnets generates noise for the EIS reading.
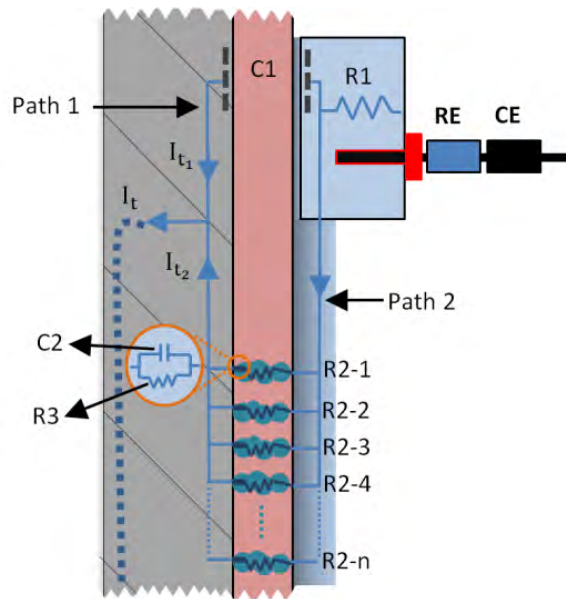
Figure 1.9: Portable electrochemical cell method for corrosion and crack detection [8].

Recent work by Nazir et al. led to the development of a portable electrochemical cell (PEC) that does not damage the coating after each test, shown in Figure 1.9. Instead of depending on the electrolyte or working cell to penetrate the coating of another potential cell in a separate location, a current is developed between these two cells to collect the impedance spectrum. This circuit now runs through the material in between both PECs where any defects are again resistors. Using Kirchhoff's current law addition to resistors (defects) in a single experiment is possible as long as

17

the current can reach the defect.

1.2.7 Radio Frequency Identification

Radio frequency identification (RFID) has been used extensively, from bar codes to identification of planes. In recent years, researchers have been exploring the possibility and capability of radio frequency identification in corrosion detection. Radio frequency identification have three essential components, two tags, and a reader. The tag usually encompasses an antenna in which it will send out a radio wave to the reader when it is energized. Tags are often divided into two kinds, active and passive. Active tags require a power source that are typically attached to the tag like a battery. Passive tags do not have a battery and are excited by the reader, which is favorable for the fields of structural health monitoring and corrosion detection[9, 68].
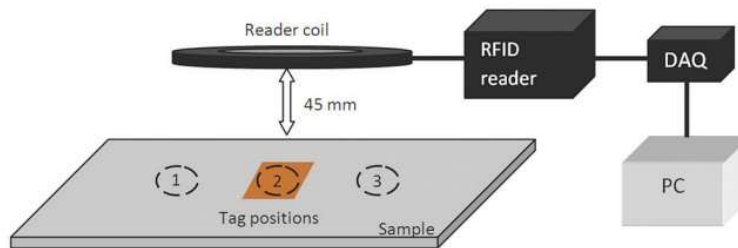
Figure 1.10: RFID for corrosion detection through excitation of a coil [9].

One approach using RFID technology is inspired by eddy current and pulsed eddy current. Above is a similar setup to pulsed eddy current, outfitted for RFID. The reader coil excites the tag which is placed above positions 1, 2, and 3. The tag will be energized through the electromagnetic field that behaves like an alternating magnetic field [68, 9]. The variable of interest is the difference in current between the reader and the tag or impedance. The limitations to this method are related to the

18

intrusiveness of implementing tags within the coating and substrate leading to crack propagation which is shown in Figure 1.11.
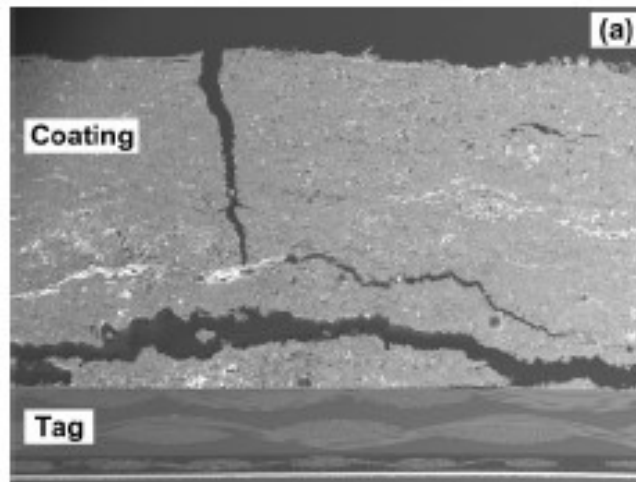
Figure 1.11: SEM of crack in coatings systems due to poor adhesion of taggin system [10].

1.2.8   Ultrasonics

Ultrasonic guided waves use a long range ultrasonic method that is currently popular in all sets of testing and fields, and is used quite often for defect detection in several mechanical structures. The equipment used are typically includes transducers and a receiver as shown in Figure 1.12. The frequency range is generally within 20 kHz – 10 MHz. Ultrasonic guided waves detect defects by emitting a wave within the aforementioned frequency range mentioned before into the substrate; as they return, a phase change of velocity within the wave will allow us to determine a defect.

19
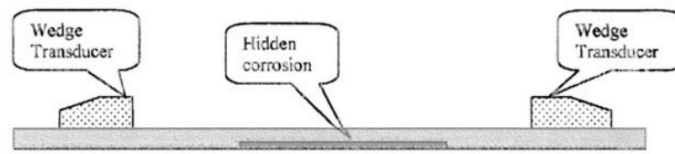
Figure 1.12: Typical setup of ultrasonic transducer systems [11].

In a study by Zhu et al. researchers investigated the radio frequency (RF) wave and its fast Fourier transform (FFT) wave that was received from a metallic plate, one which contained corrosion and one which was absent of it [11]. A manufactured corrosive damage had been analyzed along with a set of corroded plates which were tested. The plate's simulated corrosive defects had various corrosion depths at 5%, 10%, and 20%, of 1.62 mm and 2.16 mm plate thicknesses. The corrosion plates were prepared with an electrochemical procedure [11]. The change of the material due to corrosion will affect its properties including a wave of time-of-flight across it. The difference of the time-of-flight between signals of the corroded and non-corroded plate can be explained with Figure 1.13. Here the (frequency) x (thickness) (fd) product is lower in the corroded sample causing the change in the group velocity shown. Aside from (a) in Figure 1.13, there is a decrease in the phase velocities for all modes as the fd product decreases. There are also changes in the group velocity modes, but the trend will depend on where the fd product of the non-corrosion is located.

(a)RF through the shallow corrosion zone(0.02mm)   (b)FFT of the RF in the left figure

(c)RF through the medium corrosion zone(0.15mm)   (d)FFT of the RF in the left figure
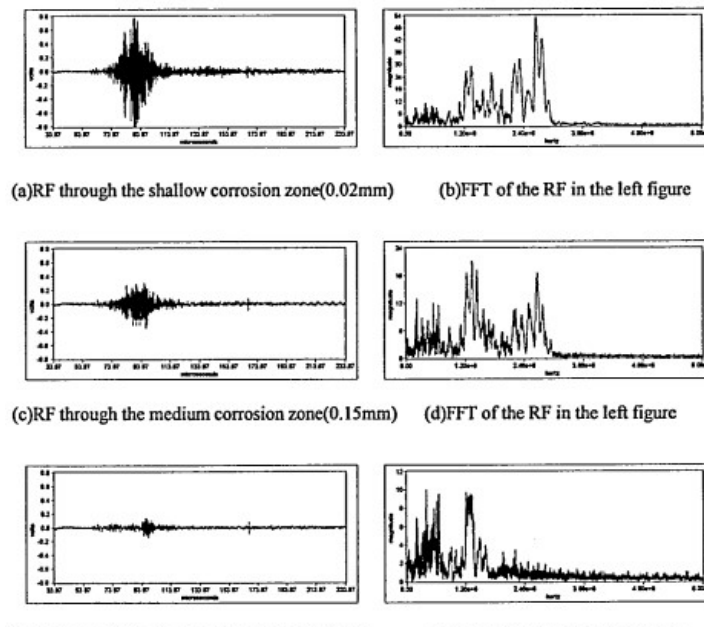
Figure 1.13: Radio Frequency and phase change with respect to level of corrosion [11].

At a certain point, the corrosion depth can cause the fd product to decrease below the cutoff value of the wave mode. The mode that falls below the cutoff fd value will be eliminated from the analysis process, which can be compensated for within the code to keep all modes. As seen in Figure 1.13, the transmission and reflection amplitude can be used to estimate corrosion depths [11]. This method requires that the surface is accessible and appropriate for the transducer to scan. Linear defects are often undetectable if they are parallel to the wave. Guided ultrasonics are sensitive to internal and external damages and have fixed inspection parameters, including fixed focal point and incidence angle [11, 69, 70]. Although it can identify the behavior, it can only do so due to the data recorded in its non-corroded state. For this method to be used as a definitive corrosion detection method, it will require a database of the material after production.

21

1.2.9 Acoustic Emission

Acoustic emission is the detection of transient waves from localized sources within a material. Acoustic emissions can often be used to locate a defect, but because many defects corroded, and non-corroded are very similar. Acoustic emissions would detect the noise of interest over long periods of time with a group of transducers. However, for acoustic emissions to detect corrosion, the corrosion process must be observed while happening. As corrosion occurs in small concentrated acidic pits within the material there is a large production of gas. The gas produced results from hydrogen bubbles breaking which highlights the corrosion process underway and results in an acoustic emission. In experiments to detect corrosion, the samples created are placed in a electrolytic solution accelerating the corrosion rate of the substrate [12, 71, 72, 73, 74].
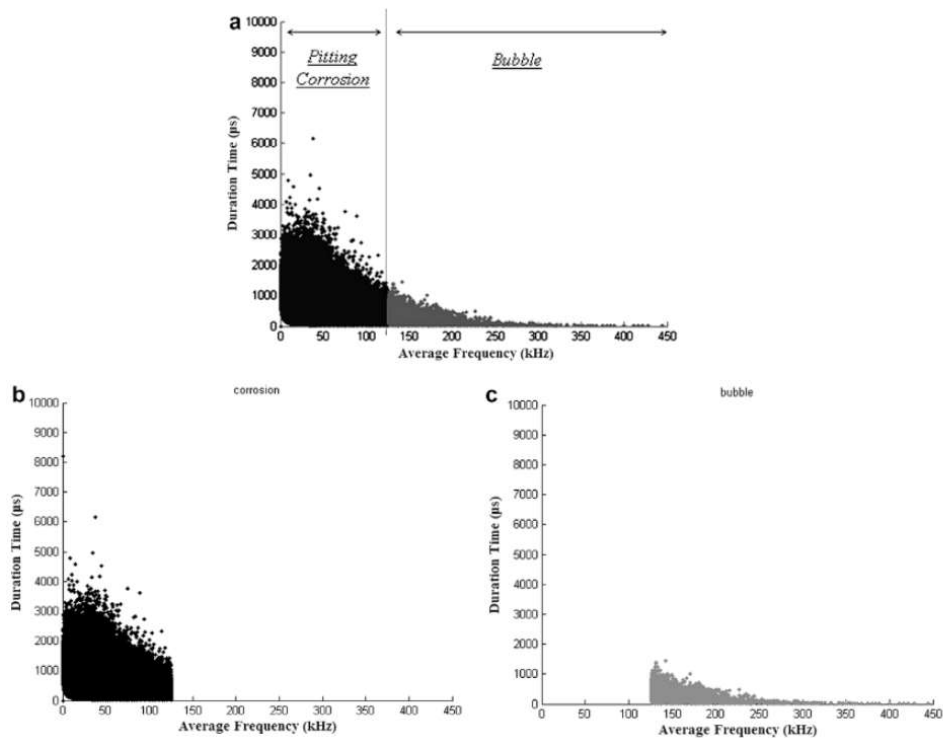
Figure 1.14: Acoustic emission results for chloride corrosion, oxide corrosion, and resonance frequency of bubbles only [12].

Research has also shown the acoustic emission sources of uniform corrosion can be distinguished in 3 different parts. First is the damage of the metal surface as corrosion begins, then the nucleation and propagation of corrosion, and lastly the bubble breaking up in the corrosion process. This can be shown in Figure 1.14. The sample used in the pitting corrosion experiment was a sheet made out of stainless steel with a size of 4 x 6 x 0.5 cm^3, and the specimen for the uniform corrosion experiment was a sheet of carbon steel with a size of 2.5 x 20 x 0.3 cm^3. By using the resonant frequency of the bubbling, researchers have isolated the acoustic emissions of the

bubbles. Detection of the acoustic activity of the bubbles will allow inspectors to detect active corrosion[12, 71, 72, 73, 74].

This method has several advantages as it does not require any sample preparation ahead of time and can locate defects within the structure. The discovery of the relationship between the resonant signal and activity of the pit allows for inspectors to locate active corrosion; however, after a pit finishes its potentiostatic step it will be detected as a regular defect with acoustic emissions.

1.2.10 Pulsed Eddy Current Thermography

One of the most unique methods due to its multi-physics background, is pulsed eddy current thermography or electromagnetic induction pulsed phase thermography (EMIPPT). Pulsed eddy current thermography is a combination of pulsed eddy current under the inspection of an infrared camera as shown in Figure 1.15.
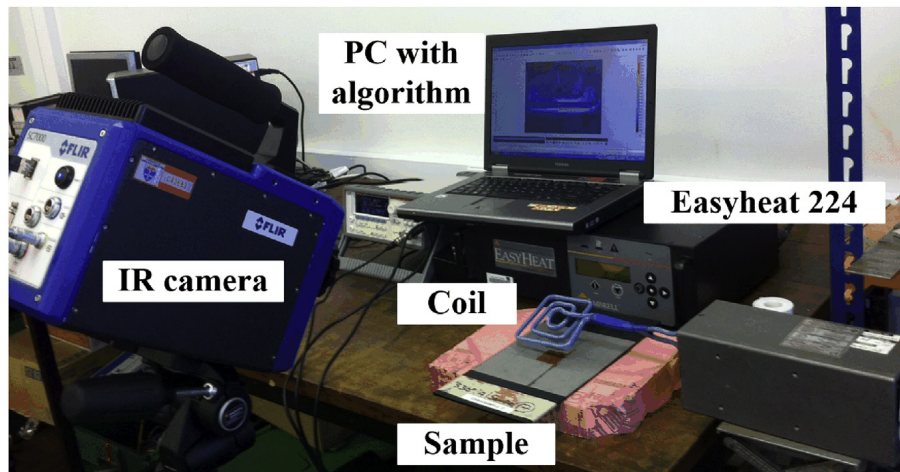
Figure 1.15: Typical experimetnal setup for PECT for defect characterization [13].

An electromagnetic coil is set at certain lift of distance and frequency depending on mode chosen (locked-in, phase, or pulsed). In PECT, the pulsed mode is favorable due to its simplicity for implementation and detection capability; however; this instrumentation can be modified with not only infrared variations, but also eddy current methods as modulated, varied, and gradient PEC. For PECT, the equations that describe the physical response of the electromagnetic field and heat generation will be discussed in more detail in Chapter 2. These equations are used to relate the penetration depth to excitation frequency in order to estimate the frequency required depending on material characteristics [13, 75, 76, ?, 58]. This technique utilizes pulses within the material through a magnetic field that will begin to induce eddy currents in the system. The eddy current in the system will begin to heat up the material and corrosion area due to the vibration of the atoms within the magnetic field known as resistance or joule heating. This can be observed with an IR camera, where temperature localization will be generated near or on defect areas [13, 15, 17, 16]. Taking the dielectric properties (magnetic permeability and conductivity) and thermal properties (emissivity and diffusivity) in consideration, material detection and changes in that material can be determined assuming 1D transient heat transfer. In this system during this heat flux change, the conductivity and change in the magnetic field of the material can also be measured for amplitude and frequency changes when coming across different defects. This allows PECT to have a higher sensitivity and resolution for shape and size of corrosion and defects compared to PEC and IRT [13, 52, 15, 17, 16, 77]. These changes can be highlighted by three different types of images that can be processed from the data collected. These images are processed for frequency or phase change, amplitude of magnetic field, and temperature changes due to localized defects, as shown in Figure 1.16.
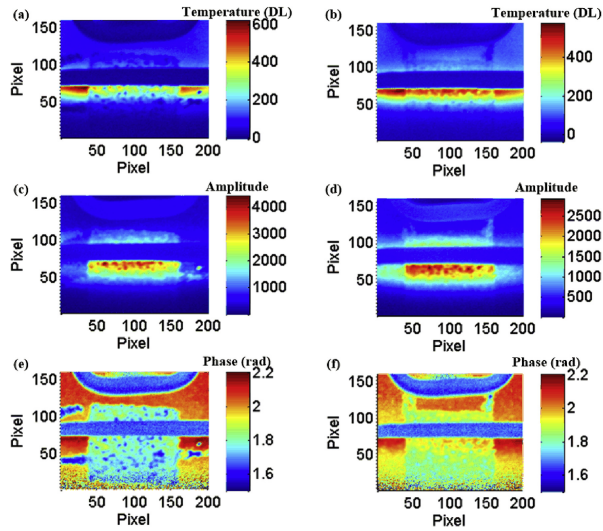
Figure 1.16: Thermography imaging of PECT for corrosion under insulation [13].

1.2.11   Evaluation of Techniques

To select a technique for research and development, an evaluation of the described techniques was conducted with respect to criteria of interest for field application. To do this, a Fibonacci scale, as shown in Table 1.3 and further detailed in the appendix, was adopted and tailored through multiple discussions with industry to weigh these criteria and establish factors to rank parameters in function of their importance. This Fibonacci scale was then used to evaluate the techniques based on in field application requirements for corrosion detection on aircraft.

Table 1.3: Example of the Fibonacci Scale used for technique evaluation. The full ranking matrix can be found in the appendix

			Fibonacci Scale		
#	Scan Time Collection	# of Sub-systems	Maturity	Area	Depth
0	Real Time	1	Industrialized method with all concepts understood	1 x 1 m	0.1 m
1	0-100 μs	1	Industrialized with very few unknown discrepancies	5 x 5 dm	50 cm
2	.2 - .900 ms	2	Industrialized with some unknown discrepancies & researched in academic settings	10 x 10 cm	25 cm
3	1-120 seconds	3	Researched in Academic setting with some discrepancies awaiting approval for testing standards	5 x 5 mm	10 cm

Each of these methods and where they stood when rated with each other, was rated using a Fibonacci scale. A matrix was developed to scale each of these based on weighted scale. Each weighted rating is added together to give a total score. Scores closer to 0 correlate to a more proficient method for on-field applications. Advantages, limitations, cost, and maturity of the method are all components that were considered for each of these NDE techniques that have been considered and evaluated. Cost, out of all the criteria, had to be roughly estimated due to lack of available information from literature. To rate cost, all methods were subjected to an in-laboratory setting to measure a simple sample; if a method was expensive in just a laboratory setting, the price to implement that method to on-the-field, real-time detection would be a larger investment than the in-laboratory setting by extrapolation. Although some equipment prices change between vendors, it is assumed that the methods with highest resolution possible based on radiation excitation, like microwave and Terahertz, are very expensive when compared to electromagnetic methods like eddy current and electrochemical cell. Based on field application itself, pulsed eddy current thermography scored best with a 3.05, whereas Terahertz scored the lowest with a score of 10.3. This is mainly because PECT displayed quick data collection with multiple results to show characterization of any kind of defect under coating while being relatively cost effective compared to the previously listed methods. However, when comparing the probability of detection for these meth-

ods, there is a different outcome. As stated for most of these methods, a defect library or some type of machine learning would be truly essential for these methods to maintain a high probability of detection of corrosion for any aircraft structure out in the field. When looking purely at which methods could detect corrosion, methods that excelled in material detection like hyperspectral imaging, PECT, and acoustic emission were the highest in the ranking for POD.

Based on field application and the design evaluation matrix, pulsed eddy current thermography was selected for research and development. This is mainly because PECT displayed quick data collection with multiple results that have shown characterization of defects, including corrosion under coating, while remaining relatively cost effective and non-time consuming. In this work, research and development of a non-destructive PECT based prototype was undertaken and will be discussed through the remaining chapters. Chapter 2 will cover fundamental and mathematical modeling of the governing equations used when coupling the electromagnetic phenomenon with heat generation in a material system of interest, as well as a summary of the current state of work for PECT. In Chapter 3, simulations applying the numerical models and schemes discussed in Chapter 2 were performed through COMSOL Multiphysics in the effort to design and predict a novel coil system for CUI. Chapter 4 will discuss the final product and experimental parameters as well as the samples used for evaluation of the prototype system's ability to measure defects for both manufactured and real corroded defects for painted aircraft panels. Chapter 5 will discuss the findings and results for Chapters 3 and 4. Finally, conclusions and future work will be discussed and summarized in Chapter 6.

CHAPTER 2: PULSED EDDY CURRENT THERMOGRAPHY THEORY AND APPLICATIONS

Before the design and modeling of a prototype for pulsed eddy current thermography, a better understanding of the physical phenomenon is needed to predict and relate temperature responses that would be probed during experimentation. This chapter will focus on the mathematical and physical understanding of pulsed eddy current thermography and an in-depth discussion on the current state of work.

2.1   State of Work

PECT is an infrared technique that uses the coupling of magnetic field excitation to generate thermal response in a material system, as shown in Figure 2.1. This active technique is unique due to internal heating of the metallic substrate, which allows the measurement of the in-depth thermal source causing the system to be captured through thermography. Defect characterization, however, has a unique advantage when compared to other thermography methods.
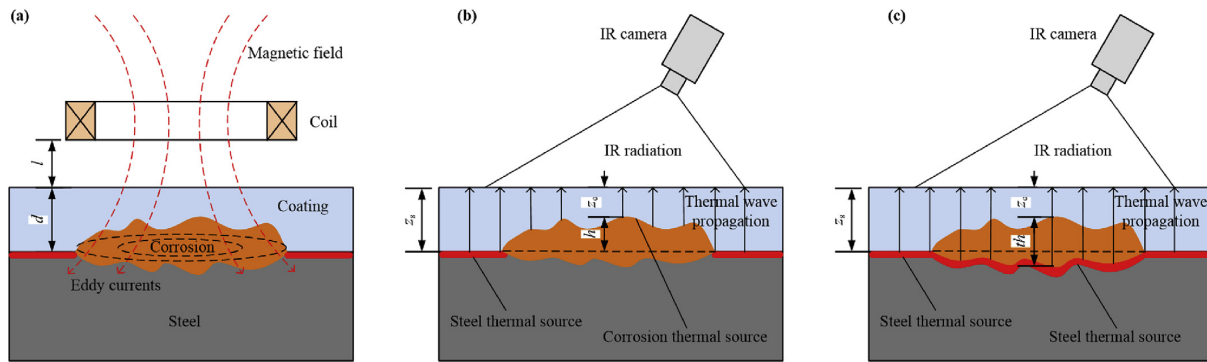
Figure 2.1: Concept of PECT for corroded defect identification and characterization [13].

The high magnitude of eddy currents in the system being generated by the induction coil can be trapped in sharp geometry causing higher resistance-heating. This phenomenon is known as edge heating, shown in Figure 2.2. This results in a localization in temperature rise in the heating face, which, not only highlights but shapes the defect of interest. Another unique aspect of this technique is that the probe volume is directly correlated to the coil geometric constraints. The coil's excitation time to generate these thermal pulses are in the magnitude of milliseconds, which allows quick time scanning periods. This allows PECT to become more modular and adaptable regarding field application. PECT, has mostly been focused on metallic structure for marine applications where metallic systems are in constant exposure from corrosive environments such as moisture and salt of the ocean [13, 15, 17]. PECT has also extended its uses for impact damage and crack detection for reinforced carbon fiber systems [78, 79].
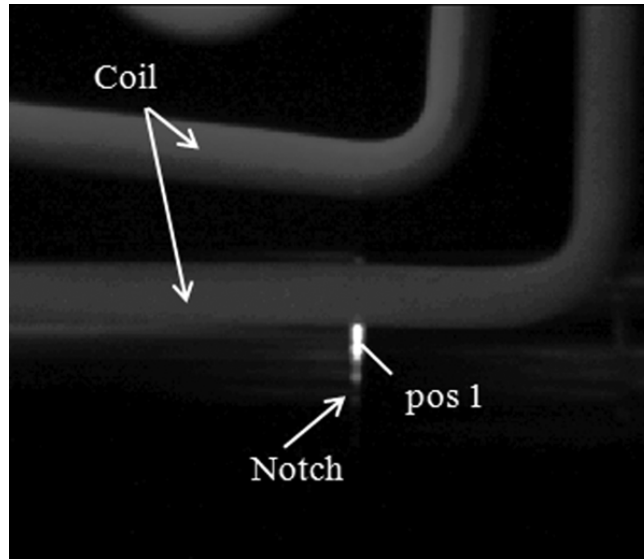
Figure 2.2: Thermal imaging of Carbon reinforced plastics characterized by PECT [14].

In most experimental testing for corrosion under insualtion (CUI), detection of corrosion can be seen in temperature windows. An extension of these measurements can be achieved through the change in phase and amplitude from Fourier transform post-processing. This post-processing results in more details such as depth of corrosion. For example, in a study done by Yang et al on corrosion characterization, PECT was implemented on steel samples coated with a paint thickness of 0.1 mm to scan a 30 x 30 μm^2 corroded area with corrosion times of 1 month and 3 months. A frequency of 256 kHz was applied to the samples with a Flir SC7500 IR camera for data collection. The generated images for this study are shown in Figure 2.3. Here corrosion for the three month sample is displayed. It can be noted the change in amplitude and phase has not only detected the corrosion but also shaped the geometric characteristics of the corroded area for one of the windows [13, 80]. Through these different "windows" or imaging schemes it is possible to increase

the probability of detecting a defect.
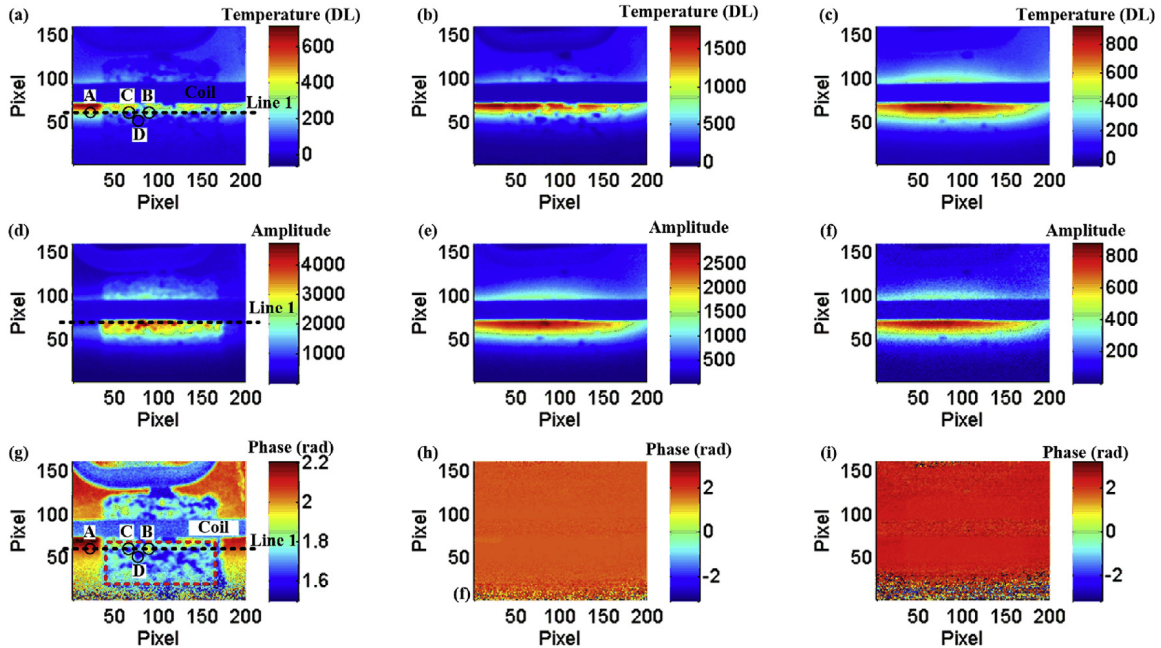
Figure 2.3: Thermal imaging of s characterized by PECT at different time steps highlighting the effects of window selection for 50 ms for (a) Temperature (d) Amplitude (g) Phase, 200 ms (b) Temperature (e) Amplitude (h) Phase, and 500 ms (c) Temperature (f) Amplitude (l) Phase[13].

Limitations of this technique are related to the non-uniform heat generation of coil geometry and increased cost due to the need of high frame rate and sensitive IR cameras. Furthermore, selection of the correct frame or temperature contrast for corrosion detection becomes a time intensive process.
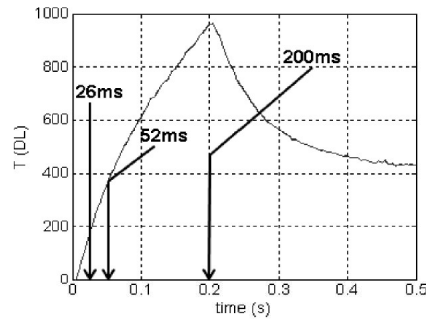
Fig. 5. Typical transient temperature change response.
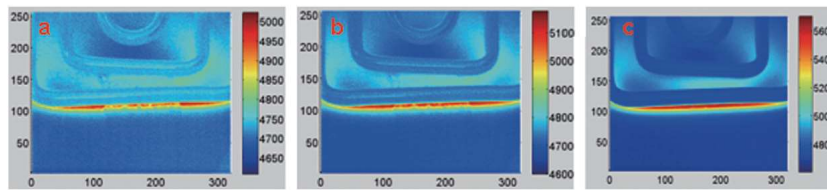
Figure 2.4: Effects of window selection with respect to time of temperature profile from pulsed induction heating with a typical transient temperature change response [15].

Contrast selection to highlight defects has been improved through recent work to automate detection, but it is restricted to only temperature contrast methods. Gao and Haung have done work implementing a blind signal separation algorithm on the transient thermal responses (TTRs) collected by the IR camera [17]. The methodology for blind signal separation involves a splitting of localized TTRs based on average peak temperature at different locations into distinct independent signal image (ISIs).

33
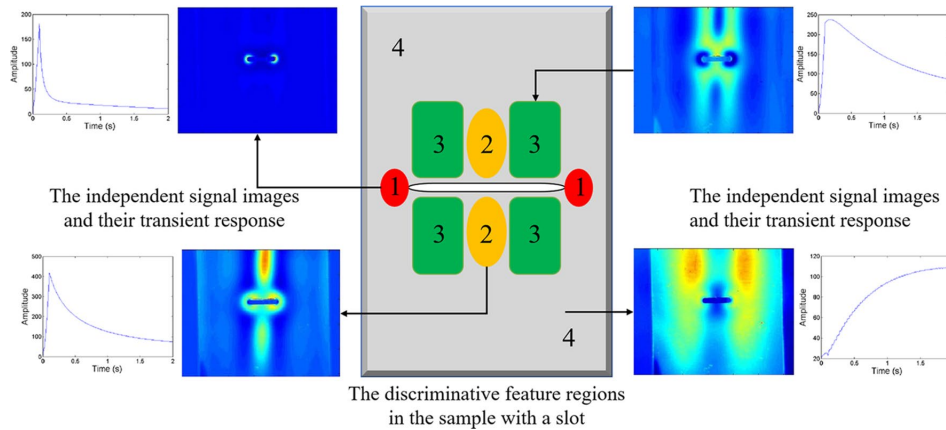
Figure 2.5: ISI generation through selection of maximum and minimum TTRs [16].

The code will begin generating data cubes based on spatial x and y coordinates of the image and selecting an optimized TTR temperature from each region with a contrast selected for that ISI region denoted in the z-direction [17, 16]. Next, it will begin using mixed modeling to average these out until optimized contrast is selected for the whole image [17]. The optimized contrast selected will highlight the defect automatically without the time-consuming process of selecting one by hand. This process can be shown with a defect on a turbine blade with the ISIs and final resulting contrast [17, 16].
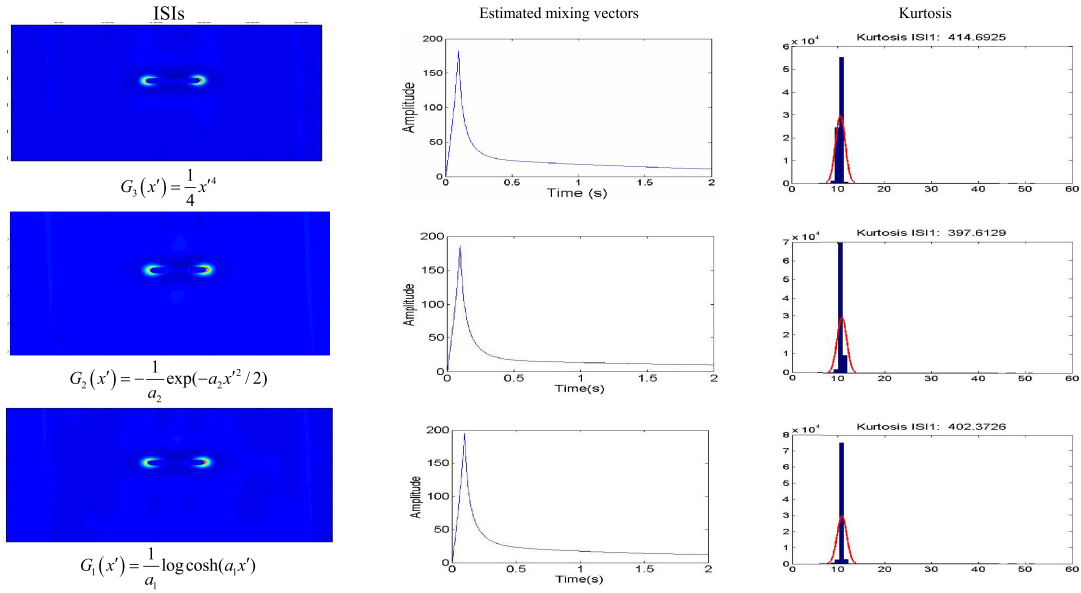
Figure 2.6: ISI vector averaging for contrast selection through Kurtosis method [17].

The automated process of contrast selection is time consuming due to the amount of frames that can be captured in one experiment. More work on automation through thermal separation patterns for phase and amplitude analysis is needed [13, 81, 14, 58, 82, 80, 17]. Overall, PECT has shown potential as a powerful technique for CUI in aerospace applications. As a new technique, most of the work done through PECT has been on non-aluminum based materials systems like steel and its alloys. The work presented here will attempt to extend the limited studies to aerospace materials and typical related corrosion defects. The ability to measure corrosive defects in fully painted aluminum alloy systems with full painted systems would be invaluable information that could lead to a new system for industry inspections, which is especially significant for the aerospace sector.

2.2   Physics and Theory

PECT uses the physical phenomenon that utilizes two major forms of energy transfer: heat trans-
fer and magnetism. Although magnetism is a force in nature and does not consist of energy, it
can transfer energy and convert it into different forms. This coupling between heat transfer and
magnetism is the major physical key of heat generation throughout material system under exci-
tation of induction heating systems. Through this heat generation, a heat profile and dissipation
pattern can be observed with respect to time through IR imaging. IR thermography, as described
in Chapter 1, works by characterizing thermal patterns that are generated by emitting light from
photons produced from the excitation of electrons. This section will focus on the establishment of
the boundary equations that will be used in Chapter 3 for simulations.

2.2.1   Electromagnetic pulses and heat generation

To produce these temperature pulses, a electromagnetic coil will take a high amount of voltage
and alternating current (AC) to produce a time variable magnetic field. This magnetic field will
penetrate a material of interest resulting in eddy currents within the material system. Eddy currents
are a result of a conductive material which is penetrated by a magnetic field, shown in Figure 2.7.
These eddy currents maintain the frequency of the magnetic field that is generated by the coil,
resulting in high frequency pulses [83, 84, 85].
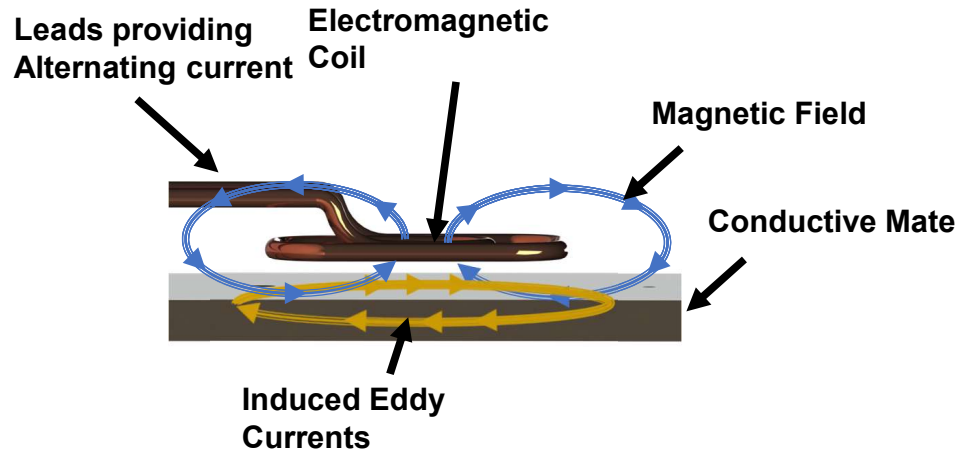
Figure 2.7: Eddy current development in a conductive material system.

These induced currents begin to form resistance heating based on the joule effect $Q_J = \frac{1}{\sigma} I J_s^2$, where Q_j is the heating from the joule effect, I is current, and R is the resistance. This coupling of two distinct physics results in large temperature changes in short periods of time. The generated heat distribution is dependent on the conductive material being excited by the magnetic field. The electromagnetic properties of different materials and the excitation coil directly impact the efficiency of these systems such as: electrical conductivity (electrical resistivity), relative magnetic permeability, dielectric constant (relative permittivity), and permittivity. Since these systems are being heated, each of these material properties change with respect to temperature as shown in Equation 2.1; ρ_0 is the initial resistivity, α is the thermal coefficient and T and T_0 are the temperature of interest and ambient temperature.

$$\rho(T) = \rho_0[1 + \alpha(T - T_0))] \tag{2.1}$$

The magnetic permeability (μ_r) is the ratio of a material's ability to conduct a magnetic flux with

respect to the medium it is in under ideal conditions. The electrical dielectric constant (ϵ) is a ratio comparing the ability of conductance of an electrical field compared to a vacuum. These two characteristics can be used to design and characterize magnetic responses that a coil may have on a certain material; however, for metallic materials the dielectric constant does not impose such an issue due to the high conductance and magnetic properties of ferromagnetic material [83, 84, 85].

For AC based magnetic fields, the eddy current distribution within a material is non uniform with respect to depth. On the surface, the largest eddy current density will occur and begin to decrease based on the magnetic properties discussed earlier; this is known as the skin depth effect. For a homogeneous material system, the estimated distributed current density can be approximated based on Equation 2.2 [83, 84, 85].

$$I = I_0 e^{-z/\delta} \tag{2.2}$$

Here, I is the current density at a depth z and I_0 is the current density at the surface of the material system, while δ represents the penetration depth of the eddy current into the material. This skin depth, based on the coil and the material system of interest can then be plotted with respect to excitation frequency f. This depth is correlated to the point where the current density is 33% of maximum surface current density. This parameter is important to track in order to understand the "range" or depth possible to probe for CUI inspection, as shown in Equation 2.8 and plotted below in Figure2.8.

$$\delta = \frac{1}{\sqrt{f\sigma\mu}} \tag{2.3}$$
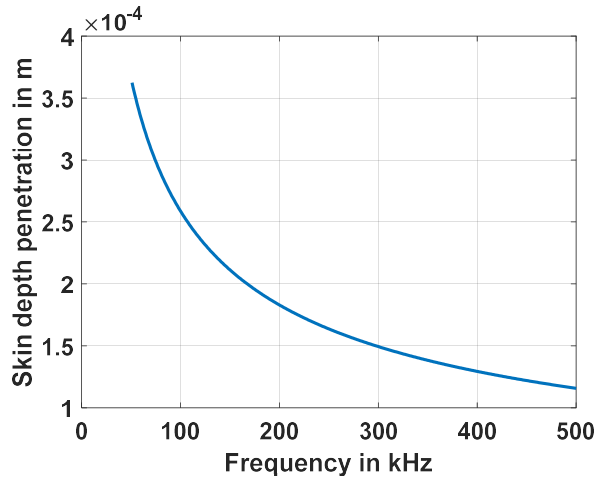
Figure 2.8: Skin depth profile for a copper coil on an aluminum substrate.

If the skin depth is greater than the thickness of the material system of interest, the system is considered electromagnetically thin. Thin bodies become semi-transparent to the magnetic flux resulting in current cancellation lowering the efficiency of the heat generation.

Similarly and related to skin depth effects, sharp edge effects are a crucial element that is observed in PECT. Edge heating effects occur when distortion of the magnetic field results in concentration of induced eddy currents due to the transverse effects of the magnetic flux on sharp geometries. There is more heat loss along edges when compared to center areas; however, edges are known to localize higher temperatures than uniform parts due to the penetration of three distinct sources of the magnetic field rather than two as long as the skin effect is distinct $\frac{z}{\delta} > 3$ [83, 84, 85].

These electromagnetic effects are coupled to heat transfer through multi-physics coupling. This is essential to understand as this method of coupling these two physics is the basis of the simulations discussed in Chapter 3. This is done first by solving Maxwell's equations from their differential forms shown below in equations 2.4 - 2.7, where E is the electrical field, D is the electrical flux

density, B is the magnetic flux density, J is the conduction current density (Eddy current denstiy in this case), and ρ^{charge} is the charge density [86, 87, 88, 17, 89, 90].

$$\nabla \times H = J + \frac{\partial D}{\partial t} \tag{2.4}$$

$$\nabla \times E = -\frac{\partial B}{\partial t} \tag{2.5}$$

$$\nabla \cdot B = 0 \tag{2.6}$$

$$\nabla \cdot D = \rho^{charge} \tag{2.7}$$

Where $\nabla \times B$ is shown below, such that the i, j, and k are unit vectors with respect to the following X, Y , and Z axes.

$$\nabla \times B = i(\frac{\partial B_Z}{\partial Y} - \frac{\partial B_y}{\partial Z}) + j(\frac{\partial B_X}{\partial Z} - \frac{\partial B_z}{\partial X}) + k(\frac{\partial B_Y}{\partial X} - \frac{\partial B_x}{\partial Y})$$

These fundamental laws become the general form of the governing equation that describe the magnetic flux and its features with respect to time in a three dimensional space, and these equations are indefinite due to the amount of unknowns in the resulting equations. To numerically solve these equations with respect to a homogeneous linear medium, three relationships between the

field quantities and material properties are defined.

$$D = \epsilon\epsilon_0 E \tag{2.8}$$

$$B = \mu_r\mu_0 H \tag{2.9}$$

$$J = \sigma E \tag{2.10}$$

Here, σ is electrical conductivity, μ_r is the relative magnetic permeability, ϵ is the dielectric constant, μ_0 is the permeability constant in a vacuum which is equal to $4\pi \times 10^{-7}$ H/M, and ϵ_0 is the permittivity or dielectric constant of a vacuum equal to 8.854×10^{-12} F/M [86, 87, 88, 17, 89, 90]. With these relations, one can simplify Equation 2.4 to Equations 2.11, assuming the displacement current density $\frac{\partial D}{\partial t}$ is negligible when compared to the magnitude of induced eddy currents if the frequency of the applied current is less than 10 MHz.

$$\nabla \times H = \sigma E \tag{2.11}$$

furthermore applying vector algebra allows for simplifying to:

$$\nabla \times (\frac{1}{\sigma}\nabla \times H) = -\mu_r\mu_0\frac{\partial H}{\partial t} \tag{2.12}$$

$$\nabla \times (\frac{1}{\mu_r}\nabla \times E) = -\sigma\mu_0\frac{\partial E}{\partial t} \tag{2.13}$$

Correlating the flux density B will lead to a satisfied zero divergence condition with respect to vector magnetic potential A [86, 87, 88, 17, 89, 90]. Utilizing this will lead to the Equation 2.14 that can be integrated to Equation 2.15, where ϕ is the scalar electrical potential.

$$\nabla \times E = -\nabla \times \frac{\partial A}{\partial t} \tag{2.14}$$

$$E = -\frac{\partial A}{\partial t} - \nabla_\phi \tag{2.15}$$

Equation 2.15 can be rewritten in respect of the excitation current density J_s in Equation 2.16.

$$\frac{1}{\mu_r \mu_0} (\nabla \times \nabla \times A) = J_s - \sigma \frac{\partial A}{\partial t} \tag{2.16}$$

To further simplify Maxwell's equations for mathematical modeling and simulation, the governing equation system can be assumed to be steady state. This leads to an adjusted governing Maxwell equations to describe the time harmonic electromagnetic field [86, 87, 88, 17, 89, 90].

$$\frac{1}{\sigma} \nabla^2 H = j\omega \mu_r \mu_0 H \tag{2.17}$$

$$\frac{1}{\mu_r} \nabla^2 E = j\omega \sigma \mu_0 E \tag{2.18}$$

$$\frac{1}{\mu_r \mu_0} \nabla^2 A = -J_s + j\omega \sigma A \tag{2.19}$$

Equation 2.17 - 2.19 are used to describe the electromagnetic current generation of the induction system. The oscillation and magnitude of the induced current J_s will be dependent on the amperage and electrical field described in these equations which then can be coupled to the heat generation within a material of interest.

The heat generation within a given material itself can be described through the Fourier heat transfer Equation 2.20, where losses of heat would be through free convection and radiation.

$$\rho C_p \frac{\partial T}{\partial t} - \nabla(k\nabla T) = Q \tag{2.20}$$

To couple the heat transfer from the induced eddy current, the eddy current density, J_s, is related to the heat generated in the system by the joule heating relation, shown in Equation 3.3.

$$Q = \frac{1}{\sigma}|J_s|^2 = \frac{1}{\sigma}|\sigma E| \tag{2.21}$$

Above is the coupling between the Maxwell simplified solutions in Equations 2.17-2.19 and Equation 2.20. These mathematical models will be applied in Chapter 3 through simulation software in order to design a novel coil system for CUI using PECT.

2.2.2   Radiation and Thermography imaging

Thermography uses temperature response of material systems that begin to emit in electromagnetic waves or spectrum, where the magnitude of emission is correlated with the absolute difference of temperature [91, 92, 93].
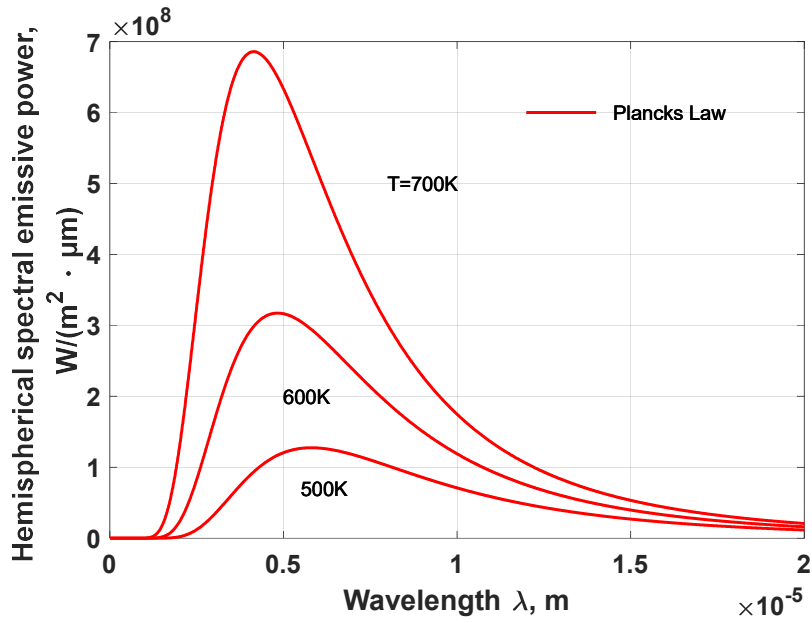
Figure 2.9: Emitted intensity with respect to wavelength at different temperatures.

This emission of discrete particles, photons, in which each photon contains an amount of energy based on the relation described in Equation 2.22. This energy will be emitted over multiple spectral bands dependent on the energy level of excitation; the spectral emissive power being emitted by a surface can be determined by Equation 2.23 [91, 92, 93].

$$e = \frac{hc}{\lambda} \tag{2.22}$$

$$I_{\lambda,T} = \frac{(2hc^2)\lambda^{-5}}{e^{\frac{hc}{k\lambda T}} - 1} \tag{2.23}$$

In the above equation, h is Plank's constant (6.62×10^{-34}), k is the Boltzmann's constant ($1.3805 \times (10^{-23})$), λ is the spectral wavelength, T is excitation temperature, and c is the speed of light.

44

Taking the integral with respect to length an emissive power in Watts can be described in Equation 2.24; however, if we assume a black body system this will be reduced to the simple solution of σT^4.

$$E_b = \int_0^\infty E_{\lambda,b}(\lambda, T)d\lambda = \int_0^\infty \frac{C_1}{e^{\frac{C_2}{\lambda T}} - 1}d\lambda \equiv \sigma T^4 \tag{2.24}$$

This emissive power is known to be dependent on the emissivity, which is the "ratio" of spectral emission for real bodies over spectral emission of a black body. This ratio with respect to solid angle direction, temperature, and wavelength can be seen in Equation 2.25. If we expand this over the hemispherical range for all angles of ϕ and θ, the emissivity in all directions (diffused body) can be described by Equation 2.26

$$\epsilon_{\lambda,\phi}(\lambda, \theta, \phi, T) = \frac{I_{\lambda,e}(\lambda, \theta, \phi, T)}{I_{\lambda,b}(\lambda, \theta, \phi, T)} \tag{2.25}$$

$$\epsilon_\lambda(\lambda, T) = \frac{\int_0^{2\pi}[\int_0^{\frac{\pi}{2}} \epsilon_{\lambda,e}(\lambda, \theta, \phi, T)sin\phi cos\phi d\phi]d\theta}{\int_0^{2\pi}[\int_0^{\frac{\pi}{2}} sin\phi cos\phi d\phi]d\theta} \tag{2.26}$$

For most emissions, the effects of change in θ are considered and the simplification of diffused grey emitting bodies will assume the emissivity only as a function of temperature. For thermography applications with small temperature changes, this simplification allows us to relate this emission with a specific temperature, resulting in thermographic imaging [91, 92, 93, 94].

These theoretical models that were described will be applied to design and prediction of temperature responses of material systems while configuring optimal coil geometries for CUI. In Chapter 3, a major focus is the design of a novel electromagnetic coil and understanding the effects of edge

heating, lift off, and current with respect to temperature response.

CHAPTER 3: SIMULATIONS AND DESIGN OF PECT SYSTEM

3.1 Design of PECT System

The two major systems that form a PECT system are the induction heating system and the thermography imaging system, and each of these components needs to be selected or designed to optimize corrosion detection. The induction system consists of the power supply and coil, while the thermography system is the thermal imager.

3.1.1 Design of the induction system

In literature, it has been seen that induction system units used for CUI maintained power ratings of 2 - 4 kW. Since the goal is to heat the material with small temperature changes the lower wattage, the more control of temperature changes can be achieved. The power system that was used is the RDO HU-2000 system as the system provided built-in excitation time and power controllers as well as internal cooling. This internal cooling would help keep the coil "dark" in the thermography images. To ensure that the coil geometry generates the appropriate heat profile and uniform temperature distribution with the selected power supply system, a novel coil was developed; this is essential as the ability to detect defects for this system is dependent on this heat generation and dissipation. There are several factors relating to the coil that affect the thermal performance on a material system, including the coil diameter, coil shape, lift off (distance from coil to sample), coil material, coil input current, and sample material when considering bulk heating. Equation 3.1 shows the relation between these properties for the efficiency of heating on a material system. This is plotted with respect to change in lift off z and coil radius a in Figure 3.1. Here σ_m and μ_m are the electrical conductivity and magnetic permeability of the material of interest while σ_c and μ_c is

the coil's material system.

$$\eta \propto \frac{1}{1 + \frac{2z}{a_I}} \sqrt{\frac{\sigma_m \mu_c}{\sigma_c \mu_m}} \tag{3.1}$$
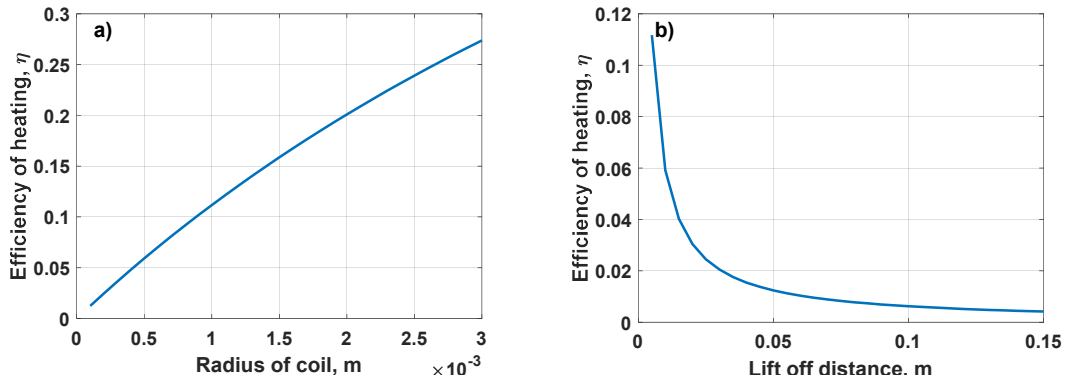
Figure 3.1: Efficiency of heating plotted with respect to coil radius and lift off distance for an aluminum substrate with a copper coil.

The material that was used for the coil was copper which is the standard typically used for induction systems. Using copper as the base material, the next design consideration was the shape and diameter of the coil. To determine shape of the coil, the consideration of the input power of 2kW is kept in mind as this will restrict the amount of turns that are possible; however, before number of turns can be established the general shape needs to be decided. The shape was chosen to be a square planar coil, as studies done by Tsopelas et al. displayed that planar coils had more uniform magnetic flux distribution [95, 96, 97]. This would lower the chances of false positives, while also lowering the intensity of the magnetic flux density which would help maintain a non-destructive hot region. To keep this shape while maintaining lower temperature and keeping the power restrictions, the amount of turns that was viable was a 3-turn based coil with a coil diameter of 3 mm. A smaller

diameter size was chosen to get sharper turns without pinching the internal cooling of the system and to optimize the coil area. Using Equations 3.2 - 3.3 a basic analytical model can be used to estimate how much temperature change would occur for a pulse of 450 ms on an aluminum substrate with a current amplitude of 380 amps. Table 3.1 displays the coil characteristics that were chosen based on the restrictions and limitations from manufacturing.

$$P_w \propto I_c^2 \sqrt{\frac{\mu_r f}{\sigma}} \tag{3.2}$$

$$Q = P_w t_p \tag{3.3}$$

Table 3.1: Final design coil parameters

Coil Characteristics			
Parameter	**Limitations**	**Justification**	**Chosen**
Material	Copper	Industrial Standards	Copper
Diameter	3 - 6 mm	Power limitation and Area optimization	3 mm
Shape	Solenoid and Planar	Uniform Heat gen Literature	Planar
Configuration	Square or Circular	Literature	Square
# of turns	2 - 4 turns	Power limitation and Area optimization	3

3.1.2 IR thermal imaging system

For the optical camera it was essential to capture as much information of the dissipation and generation of heat. Due to the pulsed nature of this system, This would require an IR camera with high

temperature sensitivity and a high frame rate. Thermal imagers can be broken up to four major categories: near infrared 0.7 - 1.4 μm, short wave infrared (SWIR) 1.4 - 3.0 μm, mid-wave infrared (MWIR) 3.0 - 7.5 μm , and long wave infrared (LWIR) 7.5 - 12.0 μm [93]. The excitation time of most PECT scans were 260 ms [46, 98, 90, 18]. Considering high speed alone, would suggest the need for an SWIR camera with high speed imaging, but SWIR does not have as high sensitivity and resolution as MWIR and LWIR cameras. From literature, it was seen that a frame rate of 300 Hz was more commonly used than lower frame rates. MWIR cameras have been more commonly found in literature for pulsed eddy current applications for both their high temperature sensitivity and high frame rate, but LWIR cameras have higher sensitivities for lower temperature changes than MWIR [80, 17, 92, 93]. Although LWIR is not as prevalent as MWIR in literature, LWIR has higher thermal contrast and are more sensitive to small temperature changes. Since the objective of this study was to perform corrosion detection with negligible effects on the material, LWIR is more favorable. Another aspect to consider was portability as MWIR and SWIR imagers are larger due to the internal cooling needed for electronics. Therefore, a LWIR camera was selected due to its compact size, frame rate of 30-80 Hz, and a sensitivity of 2 mK (Micro-Epsilon thermo-imager 450).

3.2 Samples for simulation and experimentation

To simulate and investigate the prototype PECT system, a set of calibration samples were developed as a basis for understanding the difference of certain parameters and how they affect thermal transient response in different material systems. These samples are manufactured with 5 different defect sizes on two material systems, Aluminum 2024 and Stainless Steel 303. Table 3.2 shows the geometric characteristics between the two different sample systems for simulation and experimental calibration. These samples were then implemented in a simulation to compare and predict

experimental results of the designed prototype.

Table 3.2: Calibration sample geometric features

Characteristic	Sample A1	Sample B4
Shape	Dog-Bone	Rectangular
Material	Aluminum	Steel
L (mm)	22.8	150.84
W (mm)	13.01	74.91
t (mm)	6.56	6.27
Defect Type	Manufactured	
Defect Location	Known	
Diameter Defect Size (mm)	3	1- 5

3.3   COMSOL Simulations and Physics Coupling

For the design validation and prediction, COMSOL Multiphysics was used for numerical simulations. These simulations take the theory and mathematical coupling of Maxwell Equations 2.17 - 2.19 with Fourier's heat transfer Equation 2.20. This coupling again can be described by Equation 3.3, shown below where the Q generated is the major source of heat within the material system.

$$Q = \frac{1}{\sigma}|J_s|^2 = \frac{1}{\sigma}|\sigma E|$$

Before implementing the coil design, 1D simulations were done to compare to literature to ensure simulation coupling was working as intended and prediction for the the modeling made physical sense. For all modeling environments, boundary and initial conditions used was an initial temper-

ature of 293.5 K with only heat dissipation of the material through conduction. Radiation and free convection losses were deemed negligible over these small periods of heating with even smaller cooling that was simulated. Table 3.3 shows the material properties implemented in COMSOL for the simulations.

Table 3.3: Material Properties used for COMSOL Simulations

Material Properties	Air	Low carbon Steel	Copper	Aluminum
Electrical Conductivity $\Omega^{-1} \cdot m^{-1}$	0	4.03E+06	6.00E+07	3.77E+7
Relative permeability	1	100	100	1
Density $g \cdot cm^{-3}$	1.225E-03	7.85	8.96	2.70
Heat Capacity $J \cdot kg^{-1} \cdot K$	1005	475	385	897
Thermal Conductivity $W \cdot m^{-1} \cdot K^{-1}$	0.0257	44.5	400	237
Thermal Diffusivity $m^2 \cdot s^{-1}$	2.12E-05	1.19E-05	1.10E-04	9.75E-7

Once the material properties and all external boundary conditions were determined and implemented in the simulation model, a current, frequency, and time for the pulse can be set as the main boundary condition. For the first simulation, a simple rectangular geometry of a steel based system with a single slot was implemented with a linear coil to reflect the efforts done by Shi et al [18]. Figure 3.2 shows that during the 200 ms pulse, temperature localization were seen throughout the edges of the defect as expected. This localized temperature around the defects act as the highlights that will be seen in thermography images to enable the detection of damage.
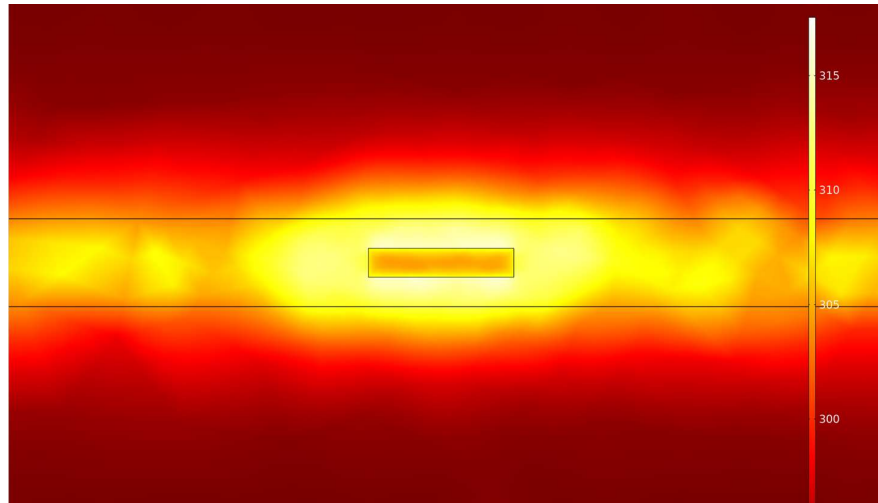
Figure 3.2: Simulated induction heating temperature contour on a "crack" of 10 mm x 2 mm x 0.6 mm at 200 kHz, 380 A, and for 200 ms.

This simulation was conducted using parameters from literature [18]. A comparison of the two simulations can be seen in Figure 3.3. It is seen that our simulation has an over estimation but maintains the similar trend. However, in these simulations it should be noted that the probed locations are likely different as it is unclear where in the part the temperature vs time plot was generated in literature [18].
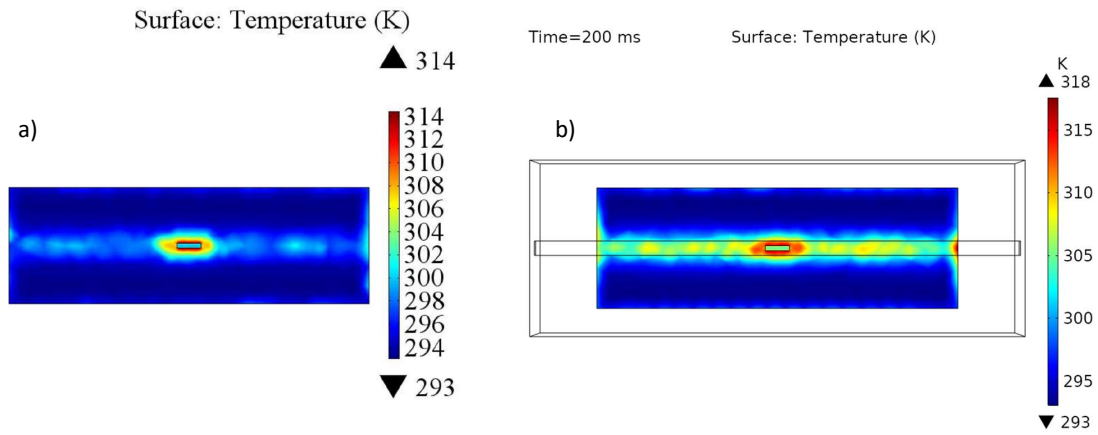
Figure 3.3: Comparison of simulations between Literature and this work[18].

To implement the coil system, a circular a 3-turn "circular" coil was used to simulate 3 turn system in a model. This coil was then set to a specific lift off, the distance between the coil and substrate. The coil was then positioned to where the tubing was placed near the defect to focus on the maximum amount of temperature change for the parametric study.
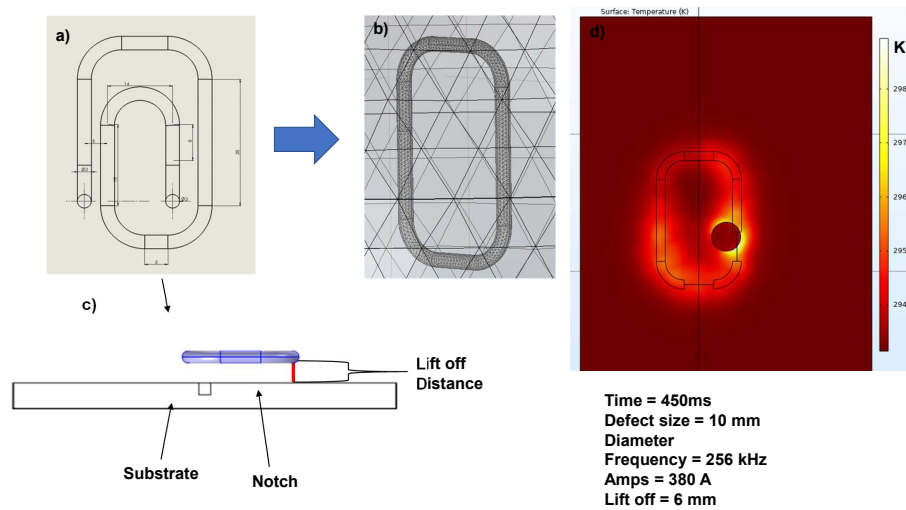
Figure 3.4: COMSOL 3D model for simulation studies, a) custom coil geometry) simplified mesh coil with (3-Turns), c) 3D model of sample and coil configuration, d) Temperature Contrast of parameters shown with significant edge heating around defect.

Once the 3D model was developed, a parametric study could be done on the three major parameters that will affect the thermal transient response: lift off, current, and defect size. Lift off, the distance between the coil and the substrate, has a direct impact to the heat generation. As the lift off increases, it is expected that the temperature decreases. Similarly, the opposite trend is expected with the current input in the coil as this will directly increase the induced eddy current density in the substrate. Therefore, the higher the current, the higher the temperature. Lastly, defect size is the most crucial parameter as understanding how the localization of temperature occurs during this heat generation can predict how geometry constraints of the defects reflect the temperature response that would be observed in thermography. Table 3.4 expresses the three major parameters used for simulations studies with respect to the parametric study of interest.

Table 3.4: Parameters used for each simulation study

Parameter	Lift off Study	Defect Size Study	Current Study
Lift Off (mm)	1 - 10	5	5
Depth (mm)	0.1	0.1	.1
Defect Size Diameter (mm)	3	1 – 5	3
Frequency (kHz)	253-266	253-266	174-274
Current (A)	440	440	88-880
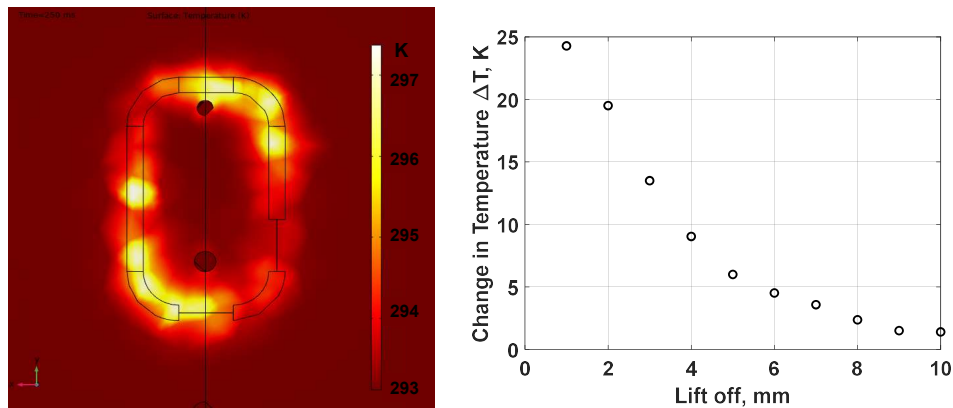
Figure 3.5: Temperature contour with temperature vs lift off plot displaying the loss in heating efficiency.

For each of these results, temperature contrasts were generated with respect to time. The maximum temperature change was then plotted at a defect. Through this, it was seen that defect edges were 2-4 K hotter than the uniform temperature rise. Figure 3.5 displays the maximum change in temperature that occurs at the edge of the defect with respect to change in lift off, and is used as a guideline for selection of a lift off that is not detrimental to the material system.
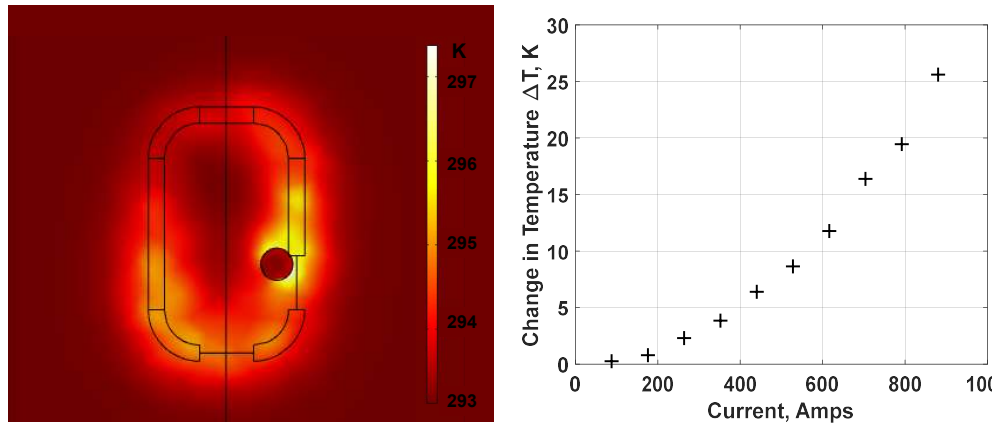
Figure 3.6: Temperature contour with temperature vs current plot displaying the gain in heating efficiency.

The opposite trend for current is seen in Figure 3.6. Using these two graphs, an optimal power and lift off can be selected for steel. Using these simulation models, predictions can be made for different defect sizes and material systems. This will help select optimal parameters for experimentation to ensure non-destructive probing for detection of CUI. Further results for these simulations will be discussed in greater detail in Chapter 5, where a comparison of the experimental studies using the same parameters from Table 3.4 will be carried out for each case. Chapter 4 will discuss the parameters used and goals set for each experimental study for this work.

CHAPTER 4: EXPERIMENTAL APPROACH FOR CORROSION DETECTION

A prototype system has been developed in this work to detect corrosion under insulation. This is done through the means of a novel excitation coil as the thermal source and a thermal imager for non-destructive PECT. To validate corrosion detection capabilities, experiments were performed on a set of calibration samples, manufactured corroded samples, and a full life cycle aircraft.

4.1   Calibration Samples

The calibration samples were tested before all other experimental scans of corrosion samples as the baseline of what is expected for defect characterization and response for a sample in which there is no knowledge of defect history. Figure 4.1 shows sample B4 with its 5 different defects with varying diameters.
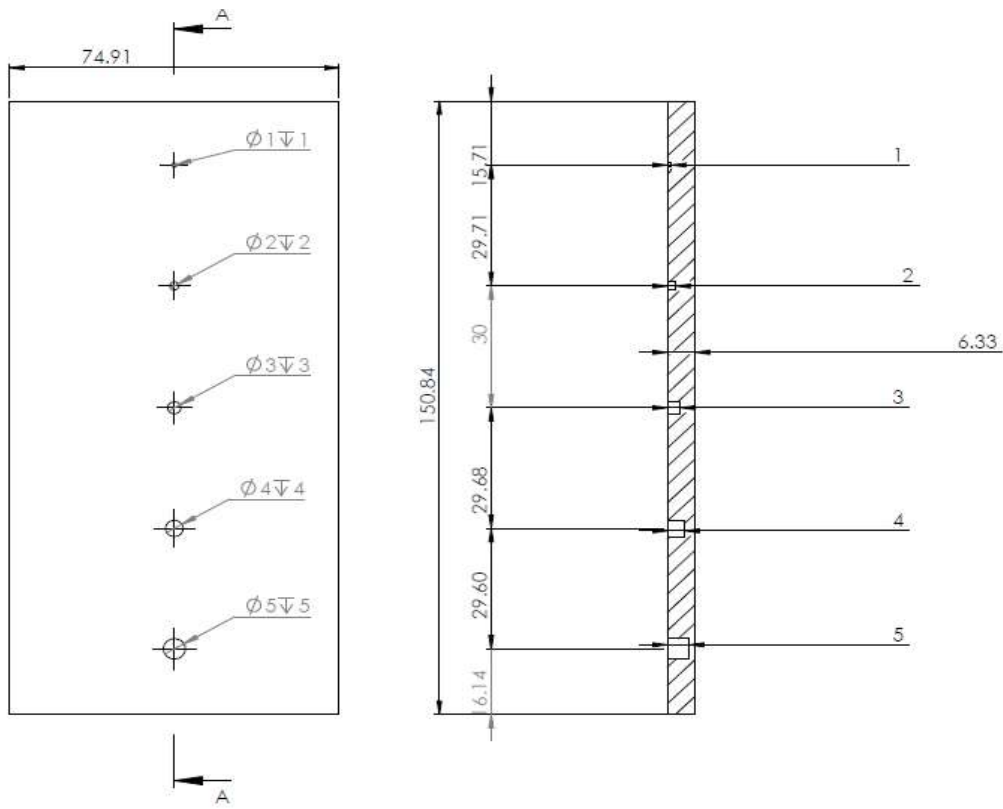
Figure 4.1: Steel sample B4 with varying defect diameter sizes.

These calibration samples follow the geometry parameters and material properties shown in Table 3.2 from Chapter 3, which will be placed below. All calibration samples were coated with 100 μm of paint.

Table 4.1: Calibration sample geometric and material features

Characteristic	Sample A1	Sample B4
Shape	Dog-Bone	Rectangular
Material	Aluminum	Steel
L (mm)	22.8	150.84
W (mm)	13.01	74.91
t (mm)	6.56	6.27
Defect Type	Manufactured	
Defect Location	Known	
Diameter Defect Size (mm)	3	1- 5

4.2   Manufactured and Corroded Samples

Samples are corroded through salt fog and electrolysis to simulate corrosion damage that would occur in aircraft systems, and one of the samples was a panel removed from an aircraft with a full life cycle. All of these panels were 6 in x 6 in x 0.5 in rectangular plates of different aircraft materials and coating configurations as shown in Table 4.2. These different configurations allow us to evaluate the PECT prototype system for effectiveness on multiple materials. The difference in coatings allows us to measure any effects of layer configurations that could play a part in measurements due to change in thickness of insulation layer. Here the top coat is 56 - 80 μm and the primer is 18 -25 μm.

Table 4.2: Material and Paint configuration for corroded samples.

Sample name	Material	Corrosion type	Side A coating(L)	Side A coating(R)	Side B coating(L)	Side B coating(R)
CA1	Aluminum	Salt-fog	Primer + paint	Primer + paint	Uncoated	Uncoated
CS1	Carbon Steel	Electrolysis	Uncoated	Primer + paint	Paint	Primer
CA2	Aluminum	Electrolysis	Uncoated	Primer + paint	Paint	Primer
CZC1	Zinc-galvanized carbon steel	Salt-fog	Uncoated	Primer + paint	Paint	Primer

4.3 Experimental Parameters

Prior to the experimentation of corroded samples, the manufactured calibration samples were tested with the same parameters as that done in simulations. These parameters, lift off and coil input current, were then optimized for experimental testing on the corroded panels. These results were used to validate the simulation's ability to predict the thermal transient response from the coil's excitation. The parameters and sample geometry can be seen in Tables 3.2 and 3.4 from Chapter 3. For these tests, 3 pulses with excitation of 260 ms were used for each location, while emissivity was chosen to be 0.9 for paint systems. The thermal imager was set up to measure the temperature changes with a full frame rate of 80 Hz.

- Lift off : 5mm
- Power outage: 50% for Steel samples and 75% for Aluminum
- Frequency: 262 kHz-272kHz (dependent on material and power)
- Current : 440 Amps
- Excitation time Time: 260 ms
- Pulses: 3
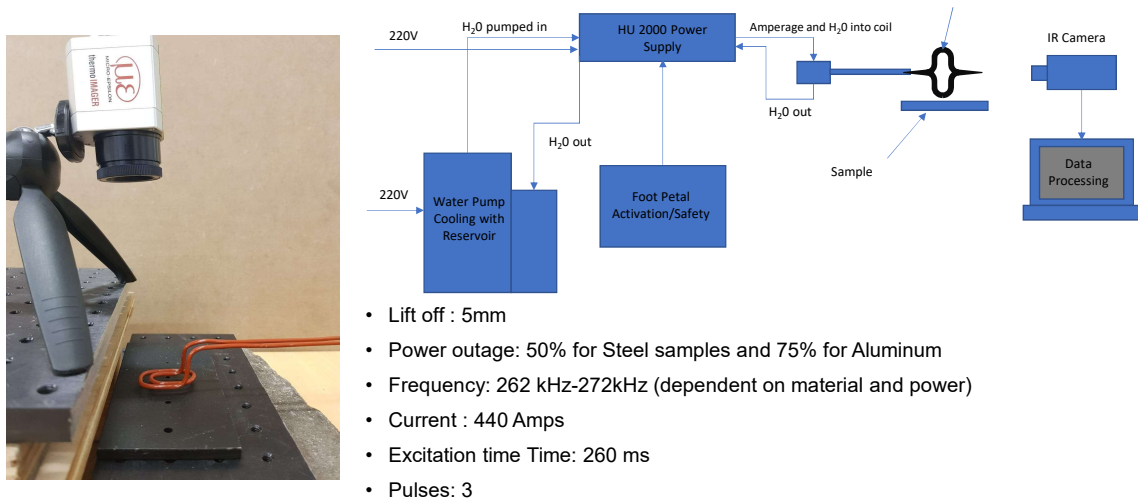
Figure 4.2: Experimental setup for calibration samples with prototype schematic.

For the corroded samples, scan parameters were developed based on the results from the calibration samples as well as COMSOL simulations, shown in Table 4.3. Four scans per side were done to measure different areas of the panels to locate defects.

Table 4.3: Parameters used for scanning corroded sample systems

Samples	Lift off (mm)	Power Output (%)	Frequency (kHz)	Exposure time (ms)	Estimated Current (A)
CA1	5	40-80	242-272	400	440-740
CS1	5	10	256	260	88
CA2	5	30	272	260	352
CZC1	5	5	176	260	44

Since the corrosion throughout the material is not visible and there is no defect map for these test samples, measurements were taken with the intent to cover as much sample area as possible. Figure 4.3 shows the scanning locations that were taken for all corrosion samples besides CA1. Scans for CA1 would be done on the whole system as the uniform corrosion is more severe. For

the corroded samples, three major capabilities were investigated for corrosion detection: visible defects vs non-visible defects, effects of insulation configurations, effects of material system, and detection during cooling and heating phase.
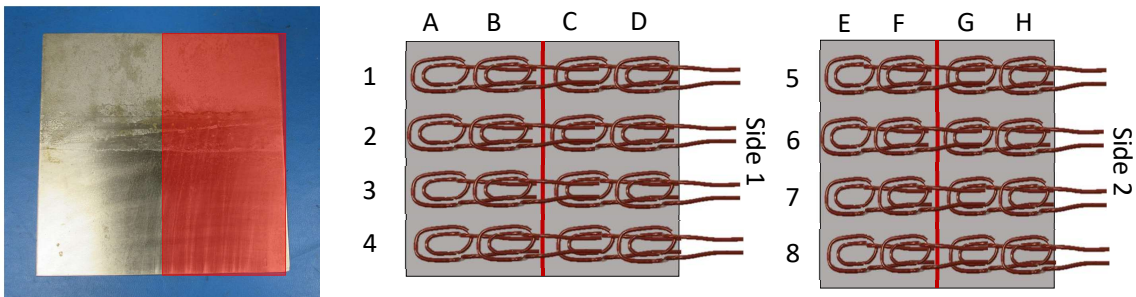
Figure 4.3: Experimental setup for calibration samples with prototype schematic.

Through these experimental parameters, the success of the prototype's ability in detecting CUI for aircraft applications will be investigated. The results for each of the thermal images will be discussed in great detail in Chapter 5, where a discussion on the calibration samples experiments will be compared with results from Chapter 3 simulations. Following this, thermal images will be discussed with regards to CUI detection. This will be seen to be insufficient and require a post-processing effort for improved defect characterization to extend PECT to a pulsed phase thermography.

CHAPTER 5: RESULTS AND DISCUSSION

Throughout this chapter, results will be discussed for areas of most interest found throughout the experimental campaign for all the samples discussed in Chapter 4. The validation of the prototype PECT system will pursue the expansion of this technique in aerospace structures. Contrast and phasegrams will display the ability that the system has to detect and identify quantitatively the shape and size of defects for multiple materials as this has not been tested before on corroded aircraft materials.

5.1 Calibration samples Thermal imaging

5.1.1 Raw Thermal imaging

After experimental testing, raw temperature IR contrast data were extracted for each scan of the calibration samples using the IR camera's software (TIM Connect). These raw temperature contrasts were first evaluated to investigate the PECT system's ability to detect and determine the shape and size of defects through change in temperature alone prior to examining the corroded samples. This also served as a comparison of maximum temperature change from the simulations from Chapter 3. The experimental results for sample B2 with defect diameter sizes of 1 - 5 mm can be seen in Figure 5.1.
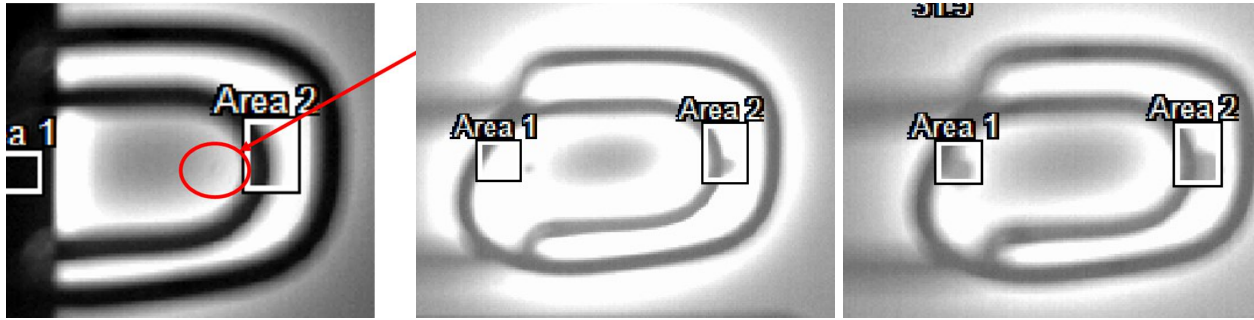
Figure 5.1: Raw temperature profiles higlighitng 1-5 mm diameter defects on coated steel sample B2.

Here it is seen that the effects of edge heating highlight the larger defects, while the smaller 1 mm defect is difficult to detect. Based on these initial scans, it can be seen that the coil's position will affect the detectability of defects. This is due to the higher magnetic flux density which occurs closer to the coil's tubing. Therefore, the scan region during the heating period becomes very dependent on coil position. Defects closer to the coil will be highlighted more depending on the geometric features of the defect. To better improve accuracy, a post-processing method to include pulsed phase thermography is needed using the dependency of the substrate's non-uniform thermal behavior to more effectively capture small damage.

5.1.2 *Simulation and Experimental Comparison for calibration samples*

Initial raw IR contrast were used to perform a comparison between the simulation and experimentation. This validation will determine inaccuracies and possible improvements needed for the simulation. Taking into consideration only the maximum temperature change at the edge of the defect, allows us to reduce discrepancies of non uniform heating and difference in probing location

between the experiment and simulation.
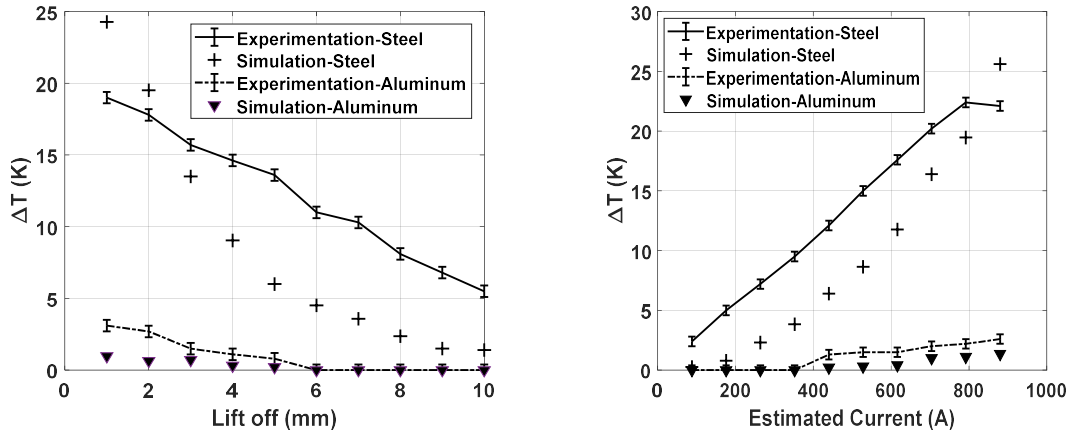
Figure 5.2: Experimental comparison with simulation highlighting the effects of change in lift off and current, while showing the underestimation of the COMSOL simulation.

Figure 5.2 shows the simulation and experimental results for change in lift off and change in coil input current. As expected, the increase in lift off will cause lower temperature changes, and both the experimental and simulated results express this trend. However, it can be seen that an under estimation is occurring throughout the simulation. This trend is also seen with the change in current. This underestimation can be linked to a few different boundary conditions and features that were not considered during simulation. The first major difference would be initial temperature of the substrate. In COMSOL, the initial temperature was set to 20°C while for experimental it was 23 - 24°C. In the simulation, different effects such as radiation, the coating, and free convection were not implemented. These differences would contribute to the underestimation observed. The results show an estimated range that can be used for the experimental setup for the corroded samples, and this ensures operators will maintain an optimal range for non-destructive probing.

For the defect diameter study, maximum temperature change of the edge was extracted from the

simulation to be compared with edge heating changes found in experiments from the calibration samples. This investigation specifically focuses on the effect of larger surface area and temperature response of the defect, as shown in Figure 5.3. For the simulation, the defect diameter size trend was not as consistent until 3 mm diameter where it begins to continuously heat up until 5 mm. The experimental results show the expected trend.
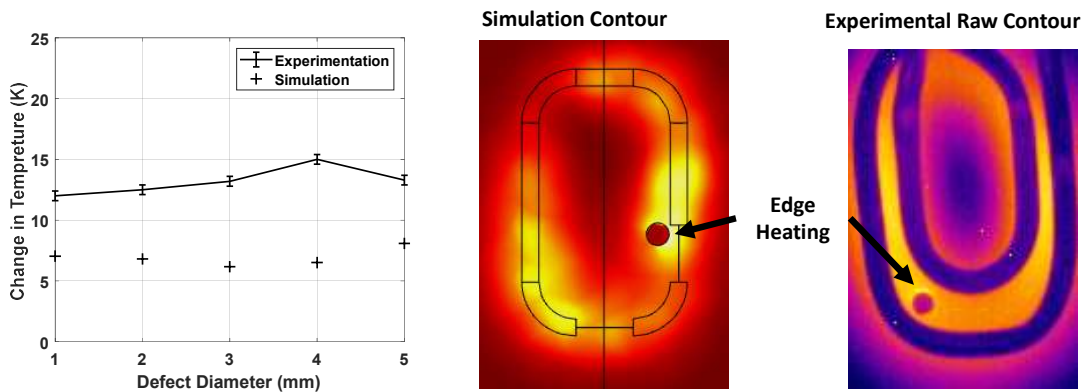
Figure 5.3: Maximum temperature change with respect to defect diameter with COMSOL edge heating prediction for 3 mm diameter defect compared to that highlighted in experimental results.

This edge heating, however, is correlated to the joule effect which is proportional to the eddy current density. This, combined with the diffused heating within the substrate, is what is used to highlight the defects. This approach is taken by other studies in literature on steel samples [15, 99]. Although the simulation depicted this correlation correctly, more work is needed to increase the accuracy to better predict defect thermal response for future experimentation and inspections.

5.2   Post-processing and automation effort

To achieve an accurate and efficient method to qualify and quantify corrosive defects, an automated post-processing MATLAB code was implemented. Following this automation, the frames selected were used for pulsed phase analysis for further characterization. Work by Gao et al, has shown tremendous effort in an attempt to automate the IR contrast for defect detection [17]. Thermal separation patterns are built through blind source signals. These patterns are built by different local maximums and minimums from the frames of interest. Through this, four optimal frames based on the differentiating averaging models will produce a single frame out of four potential contrasts. This algorithm was implemented on the calibration source first to ensure functionality. For calibration sample B2, the algorithm generated four possibles frames as the optimal shown in Figure 5.4; this proved to be effective with the larger defects of 3 mm diameter and greater on the calibration samples, but required 2 - 3 hours of run time before achieving the optimal contrast.
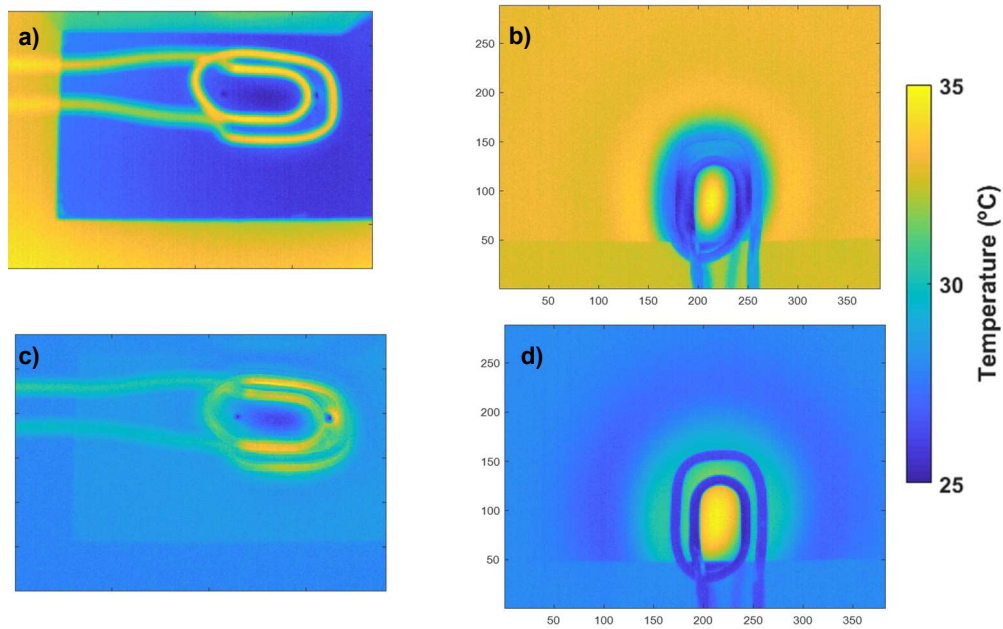
Figure 5.4: Blind source algorithm applied to calibration coated sample B4 resulting in the optimal frame (c) greatly highlighting the defect.

This time-intensive algorithm would still not be sufficient enough for detection of the aircraft or corrosive panels. The post processing for these samples was roughly 3 - 4 hours. The resultant contrast provided insufficient information for high probability of detection, especially for small defects of sizes 2 mm or less, which is shown in Figure 5.5.
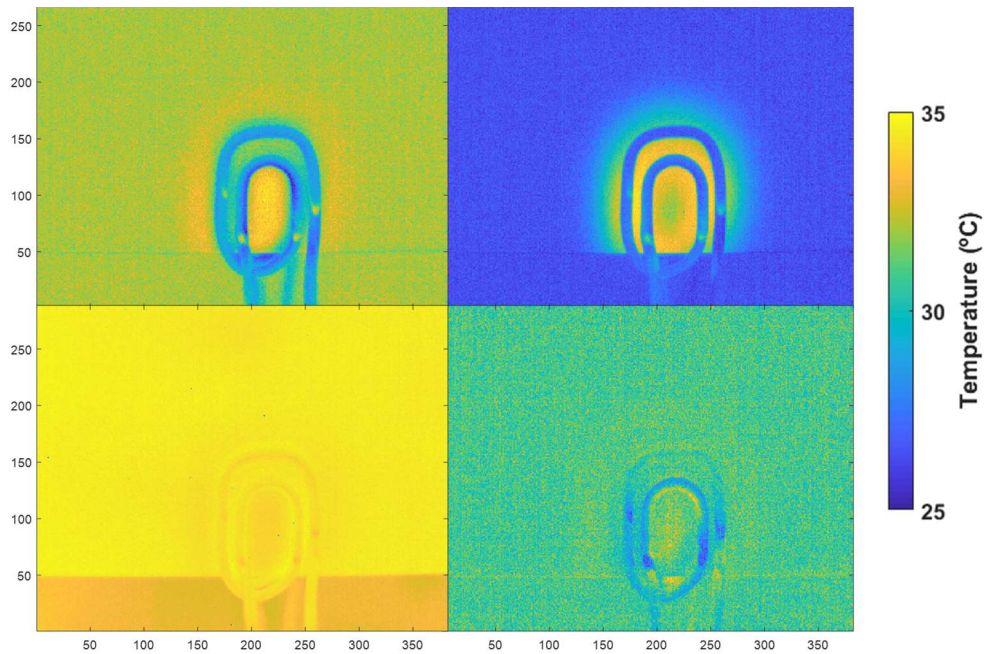
Figure 5.5: Blind source algorithm applied to corrosion sample CS1 (coated steel panel) resulting in the optimal contrast in the bottom left with insufficient information.

To increase efficiency, a code was developed to focus more on detection under insulation. By applying a discrete Fourier Transform, the thermal pulse can be decomposed to individual sinusoidal components [100, 101]. For planar sample surfaces of the substrates, multiple heat waves are being generated throughout the substrate. Each of these waves can be broken down and characterized through time and frequency domain. The time domain would be the thermal transient response used in the earlier sections while the decomposed frequency domain would focus on changes in phase amplitude of these produced waves, as described in equations 5.1- 5.3; Δt is the time between each frame, k is the thermal conductivity, ϕ_n is the phase or lag of the thermal wave, A_n is the amplitude of the thermal wave; Re_n and Im_n are the real and imaginry numbers developed by the discrete Fourier Transform decomposition. This extension generates a significant increase in

computational time for data post processing through MATLAB.

$$F_n = \Delta t \Sigma_{k=0}^{N-1}(T(k\Delta t)e^{\frac{-i2\pi nk}{N}}) = Re_n + Im_n \tag{5.1}$$

$$A_n = \sqrt{Re_n^2 + Im_n^2} \tag{5.2}$$

$$\phi_n = tan^{-1}[\frac{Im_n}{Re_n}] \tag{5.3}$$

5.3   Pulsed Phase thermography results

Prior to employing this on the corrosive panels, post processing was done on the frames from the calibration testing of sample B4. This would generate the baseline of expected trends. Figure 5.6 displays the 4 generated contours produced by the novel MATLAB code. For each of these contours, a quantitative and qualitative approach can be used for defect characterization. This characterization or detection effort can be broken down into two major periods with five distinct windows of detection for each period. These two major periods would be denoted as the heating and cooling while the five potential defect detection windows are the following: temperature, change in temperature, amplitude, phase, and change in phase.
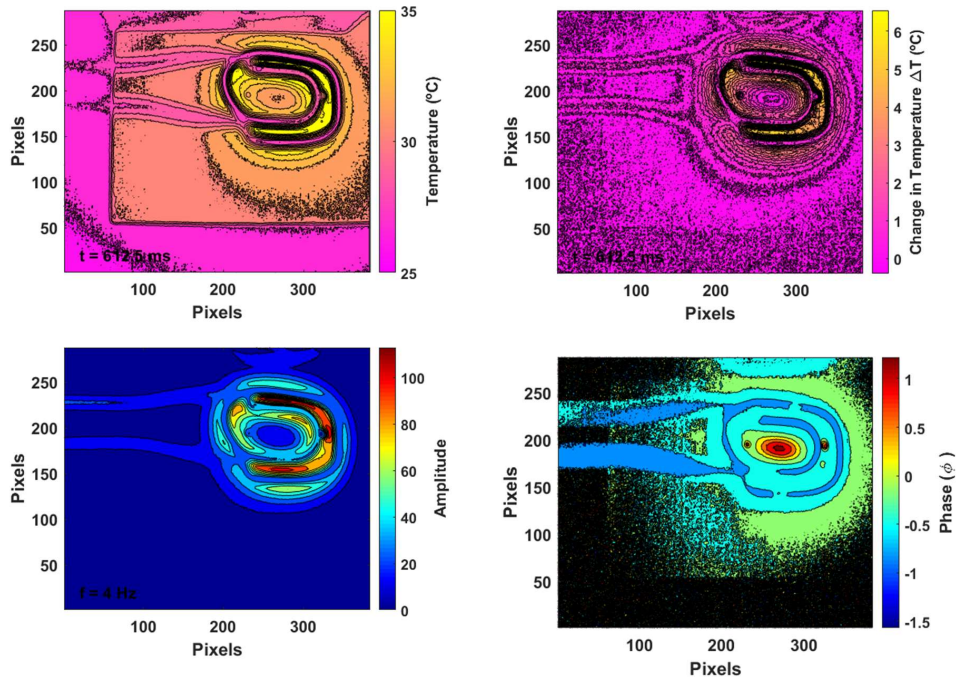
Figure 5.6: Thermographic windows generated during the heating period for the calibration coated steel sample, B4. Where (a) is raw temperature, b) is change in temperature, c) is amplitude, and d) is change in phase.

Through this extension, the defects are not only demonstrated to be detected but have also been geometrically identified. This is crucial when evaluating an aircraft part as the crevice corrosion or stress corrosion defects appear more as cracks while the localized corroded voids or pits will appear as "holes". In both the amplitude and change in phase, the shape of these "pits" are defined. With this current setup, the resolution between each pixel is roughly 300 μm. The defects with respect to bulk heat wave diffusing through the system had lags corresponding to the defects for the 3 mm which had a phase of 1.141 rad, while the 4 mm had 0.928 rad. This phase would be 0.3 - 0.5 rad larger than the uniform phase region around it. The characteristics of these phase and its

changes are directly related to the substrate material and depth of the defect. This is expressed in Equation 5.4 where a relation between the defect depth and the diffused heat will directly affect the phase measured by the camera. Where z is the depth within the substrate and μ_w is the diffusion length based on the material properties of the substrate.

$$\phi_n = \frac{z_s}{\mu_w} \qquad (5.4)$$

However, this would still be heavily dependent on the edge heating effects of the defect to shift the phase large enough to be detected. Furthermore, the change in phase and amplitude, like the temperature and change in temperature windows, are dependent on contrast selection. Unlike the temperature time domain windows, these frequency dependent contrast images will affect greatly what can be detected. Once a baseline understanding of how these defects would respond with respect to phase and amplitude was established, the investigation on the severe corrosion panel was performed. This severe corrosion sample would validate the ability to detect corrosion typically found on aircraft. Figure 5.7 shows the three major windows using different post-processing parameters for a specified period for a defect of interest on the corroded aircraft sample.
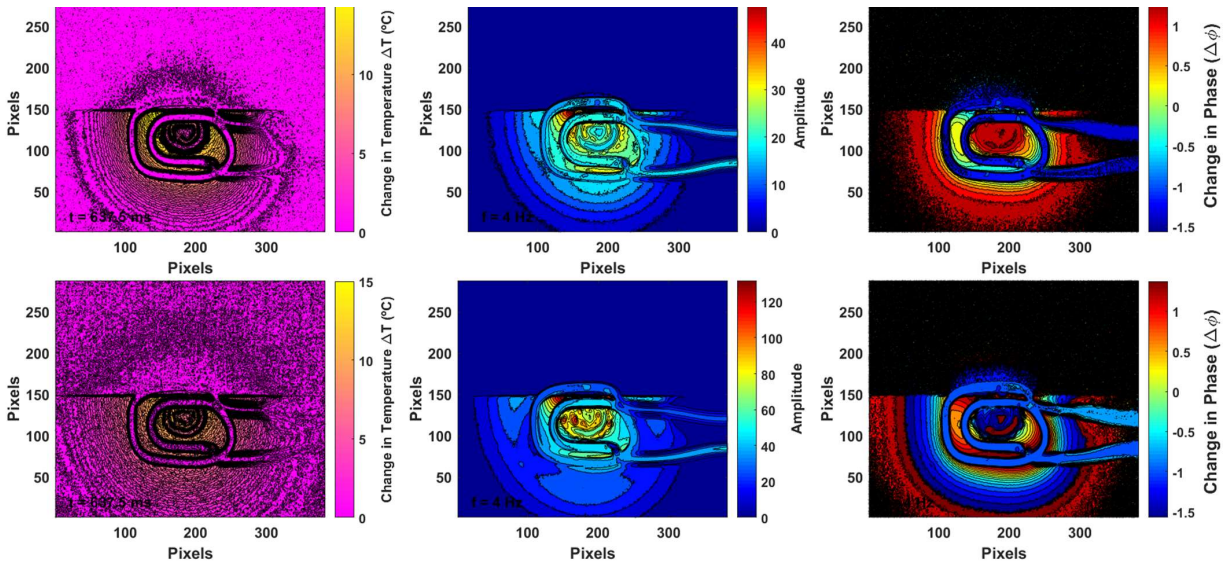
Figure 5.7: Temperature, amplitude, and change in phase for a coated aluminum alloy aircraft panel CA1 highlighting defects within blister region for heating and cooling.

Profiling of the blisters through temperature distribution details the heat diffusion throughout the blisters where points near the edge of the blister show signs of localization. High temperature changes of ΔT of almost 10 - 15°C around the major heated region with areas of the blister shows lower temperatures. This lower rate of diffusion is credited to the lower thermal conductivity within the voided region which when coupled with the edge heating effect results in changes in the lag of the thermal wave. Micro-blisters and features such as voids can be seen highlighted through the amplitude and phasegrams which was not visible through initial temperature means. Underlying blistering and pitting could occur through continuous corrosion of the sample.
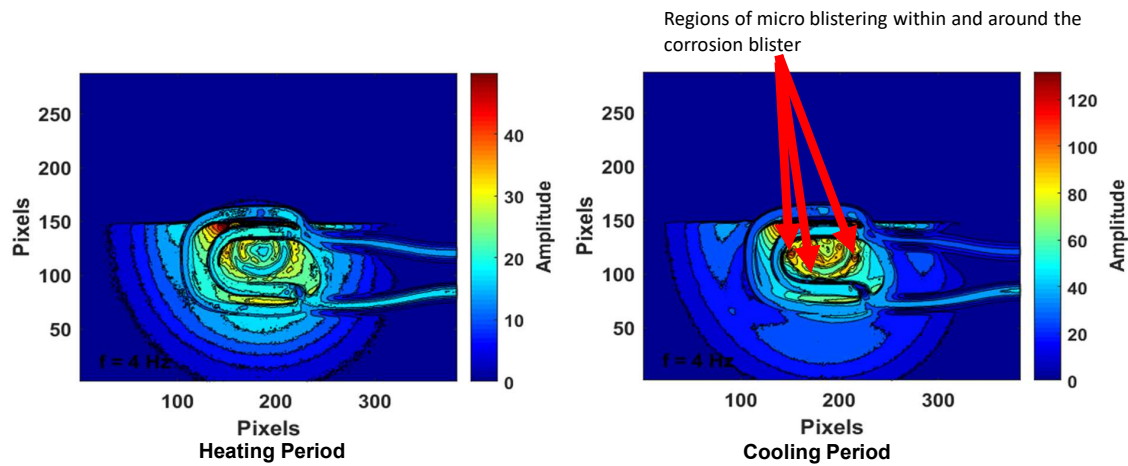
Figure 5.8: Amplitude contrasts imaging for heating and cooling period of the coated CA1 sample displaying the micro blistering underneath larger blister.

However, the temperature contrast is not sufficient enough for the characterization of the defect. For example, in Figure 5.8, the amplitude shows localization of possible micro-blisters and pitting voids underneath the major blister of interest. The amplitude and phasegrams shape the micro-blister and voids quantitatively with radii of roughly 0.5 - 1 mm. This successfully demonstrates the ability to distinguish shape and detect corrosive defects under insulation for aircraft systems. An important observation was that the cooling period of this feature highlights these smaller defects greater than the heating period. This will be seen and discussed in more detail later in this chapter.

5.3.1 Visible vs non-visible

Besides demonstrating the detection of corrosive defects on aluminum and aircraft related materials, the current method was investigated to show the capability to detect early onset corrosive damage which is non-visible to naked eye. To achieve this goal, inspection of locations with non-

75

visible damage were investigated. Corrosion damage that is sub-to near surface will begin to pit and localize without signs of flaking and blistering until much later in the life cycle. This localization will lead to cracks and loss in structure integrity. The impact that early detection of corrosive damage on aircraft structures would provide is invaluable. Figure 5.9, shown below, displays sample CS1 where there is not a defect visible for visual inspection. However, through the extension to pulsed phase thermography for PECT, potential defects were highlighted underneath this layer of insulation.
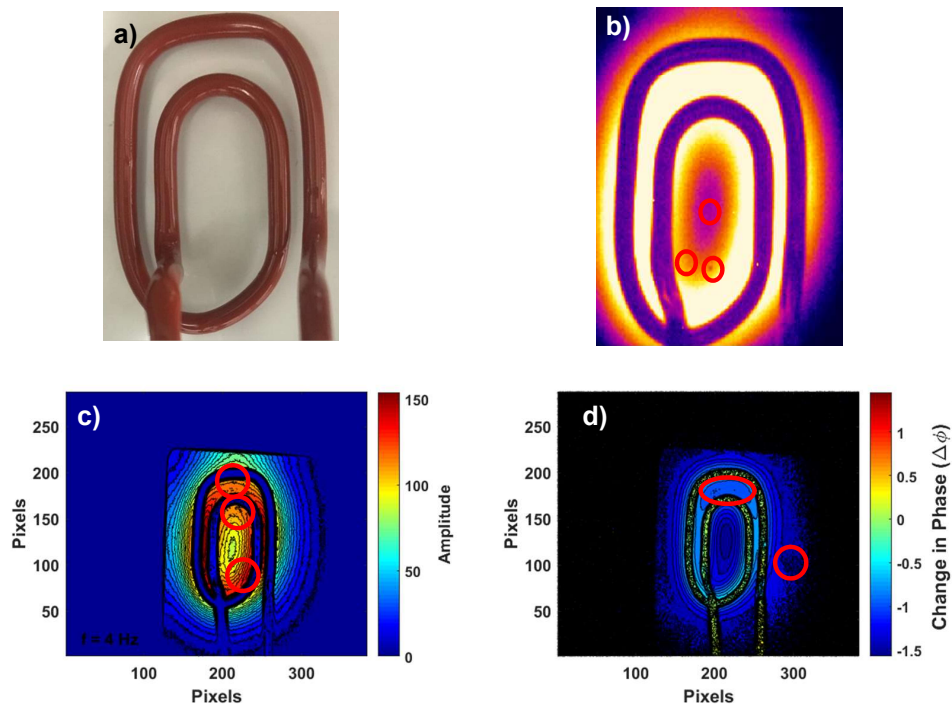
Figure 5.9: Defect detection of non-viable area for coated carbon steel sample CS1 displaying defects that are detected for a) visible image, b) raw temperature, c) amplitude, d) phasegram

5.3.2   *Change in coating configuration*

When considering multiple or different painting layers, defect detection with respect to coating configuration shows no sign of major hindrance. The coating's contribution of thermal conductivity and radiative properties would only apply very marginal changes to the ability to detect damage using this method. Figure 5.10 displays two distinct areas of the coated zinc galvanized steel sample CZC1. The first area is coated with a full coating configuration of primer and paint while the second probed area was only coated with primer. For both temperature and phasegrams, potential defects are highlighted in Figure 5.10 with red circles. Regions of interested had appeared in both windows for primer and full coating. These phases were roughly 1.14 rad similar to that seen in phase of the calibration samples, demonstrating the negligible effects of the different coating systems on detection of damage on the material substrate.
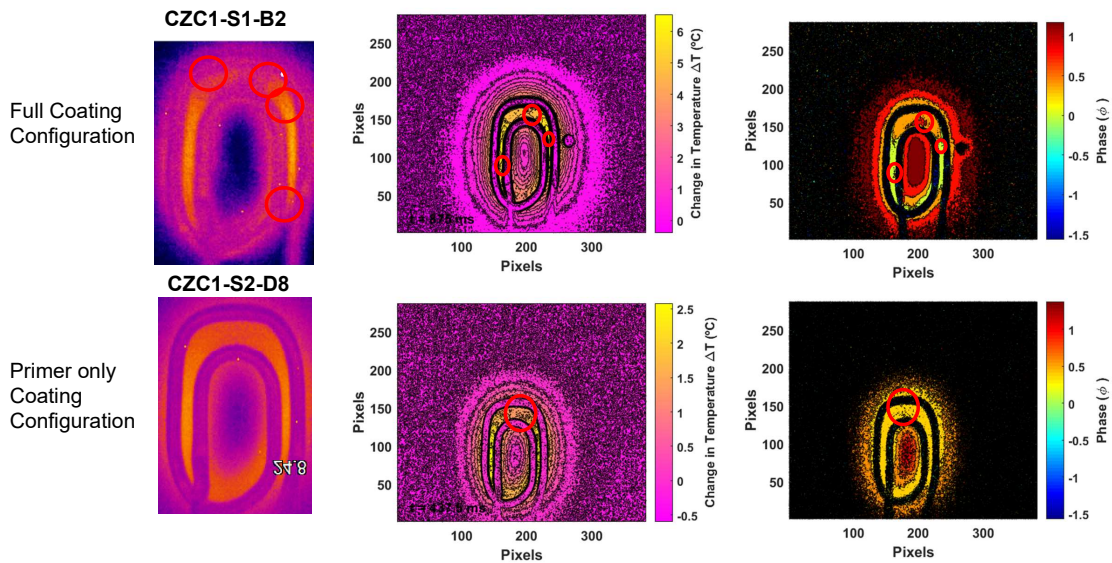
Figure 5.10: Temperature and phasegrams highlighting potential defected areas with red circles for two different coating configurations for coated zinc galvanized steel sample CZC1

77

5.3.3 Change in material substrate

In all material systems that were scanned, adjusting the necessary lift off or power was required to ensure non-destructive probing was achieved. Through COMSOL, optimal ranges of parameters for each of the panels were initially selected as described in Chapter 4. However, sample CZC1 scan parameters were altered to an estimated 44 A of input power after experimental testing due to its high ferritic characteristics. Defects were detected on all different substrates through heating and cooling as shown in Figure 5.7 - 5.10, where the contours of the three different material systems highlight regions of potential defects in multiple windows. This tailorability of the coil parameters allows for the novel prototype to probe multiple material systems regardless of coating configuration.
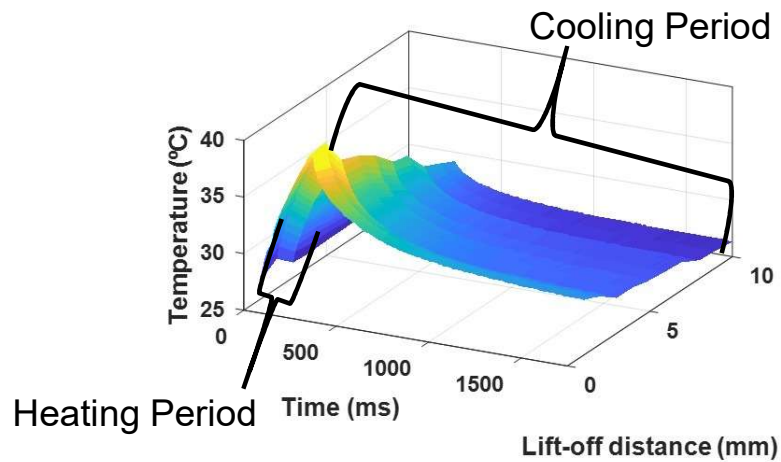
Figure 5.11: Pulses generated with respect to time and lift off distance displaying the heating and cooling period for each of these probing intervals.

One of the most significant observations seen throughout the experimental investigations was the effect of cooling and heating on the detectability of corrosive defects. The heating period defines the moment where the coil's magnetic field is generating the joule heating, while the cooling period is the diffusion of that heat throughout the material system, shown in Figure 5.11. The edge heating phenomenon occurs when multiple electrical field penetrations of the defect area causes transverse magnetic fields and increases the localized heat. In Figure 5.12, the corroded aircraft panel had regions of major defects with larger sizes and blistering, which is easily detectable during the heating period.
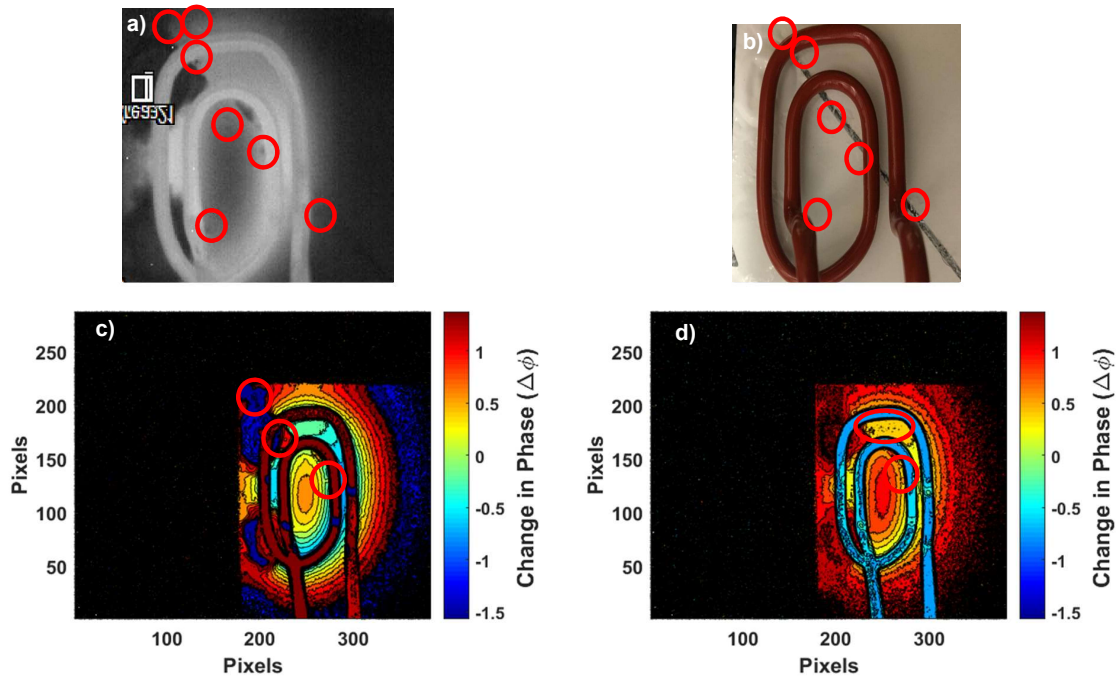
Figure 5.12: Temperature and phasegrams of sample coated aluminum sample CA1 a) Raw initial temperature contrast, b) visible image of defect area, c) change in phase during the heating period, d) change in phase in the cooling period.

When this heating period occurs, all large defects, small defects, and substrate will begin heating. However, due to the lack of captured eddy currents the smaller defects will localize very slightly and the thermal response will blend with the bulk system. These thermal waves would then result in small phase and amplitude changes with respect to the defect because the larger defects can capture more eddy currents. This is also attributed to the larger voids causing slower heat diffusion within the heat generation period, resulting in larger "gaps" of lower temperatures. However, during the cooling period defects are highlighted during the change in phase that were significantly smaller and hidden during heat generation. This is related to the change in thermal conductivity between

the material substrate and the loss in material system leading to pitting and voids. This will cause the lag in the phase of the thermal wave diffusing throughout the system, shown in greater detial in Figure 5.13.
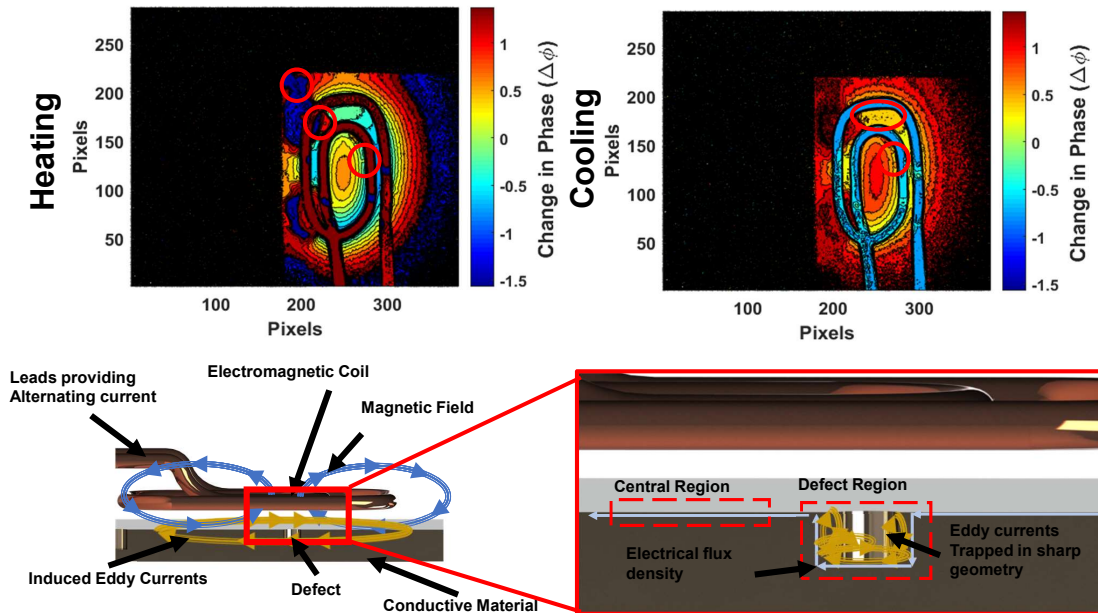
Figure 5.13: Phasegrams highlighting the defect regions from corrosion showing defected areas with phase changes of 1.12 rad and higher with the concept of edge heating phenomenon.

This diffusion was hidden during the heating period as the larger phases were generated in the larger defects around the major blisters. During cooling, this diffusion is continuous and more uniform in its dissipation, enabling the ability to highlight the smaller potential corrosive defects. This assessment of multiple windows is a powerful characteristic of this post processing method. Four potential windows in each period for one frame of the pulse probing the material system allows PECT to be more sensitive and maintain a higher probability of detection for these aerostructures.

5.3.5   *Summary of Results*

In summary, the PECT system was able to detect defects in multiple material systems regardless of the coating configuration for aluminum alloy, zinc, galvanized steel, and low carbon steel. This was made possible due to the adaptability that can be done through altering parameters such as lift and current and by capturing effects of change in thermal and magnetic properties of any of the materials. Defects from 2 - 5 mm were successfully captured through change in temperature, however through the extension to pulsed phase thermography defects of 0.5 - 1mm were detected through amplitude or phase imaging. In most cases, phasegrams and amplitude imaging had better detection of geometric features of damage and detection of corrosive defects. Through these multiple post processed windows, amplitude, change in temperature, and change in phase, distinguishing defect characteristics is made possible. For larger defects, it was shown that the heating period had identified the damage and detected the shape more efficiently, whereas the smaller defects were only sensitive to detection during the cooling period. This was attributed to the coupling of the two physics in the heat generation period. In this case, smaller defects would not generate sufficient localization blending with the bulk heat generation. This would provide the cooling period a more sensitive window for corrosive defect detection. The ability to generate multiple windows per frame of the thermal response allows for higher probability of detection for corrosive and non-corrosive defects. This investigation provides insight on the first application of PECT on corroded aircraft materials with coating configurations for detection of CUI.

CHAPTER 6: CONCLUSIONS AND PERSPECTIVES

6.1   General conclusions

This work was aimed to extend the application of PECT for the detection of corrosion under insulation in aerospace materials through simulation and experimentation considering collection parameter as well as data post-processing. To address this extension, a novel coil was designed to capture an area with respective depth for near to subsurface corrosion detection. Through COMSOL simulations, an evaluation and prediction of parameters defining the coil system for two different materials and defects were performed. These estimated temperature changes that would be produced through the electromagnetic excitation were simulated for different parameters that affect heating efficiency such as coil input current and lift off distance. Once finalized, the equipment was constructed for experimental investigation. This coil, coupled with a LWIR sensitive camera, was tested to investigate aerospace materials with different coating configurations to evaluate the capabilities and limitations in detection of CUI. Defects as small as 0.5 mm were detected through the use of phase contrast in all the different material and coating configurations studied in this work. Although aspects of the heat transfer within the material systems differ between different ferritic, radiative, and thermal properties, thermal transient responses were still detectable and characterized. Defects that were smaller than 2 mm were difficult to detect during heating periods or using initial raw temperature scans. Through phase analysis and amplitude, smaller defects were characterized. A significant finding was that smaller defects were observed more accurately during cooling period as compared to the heating period. This is due to the heat diffusion of the generated thermal waves that can hide thermal responses from the smaller defects. This extension of PECT to aerospace applications provides invaluable information on the expected thermal transient responses one would expect for corrosive defects on aircraft materials specifically under

coating/insulation.

6.2   Future work

In summary, the PECT scans have detected corrosion under insulation for all material systems for unseen corrosion defects and advanced corrosion blistering. Regarding the post-processing results, it should be discussed that for all plotted profiles manual input was needed to select frequency and frames of interest. This process can lead to timely post-processing and is still dependent on the judgment of the user comparing the contrast of phase and amplitude. For a disruptive technique, there is a need for software engineering in development of not only automation of data analysis but also probability of detection by means of the development of a defect library and machine learning. Furthermore, future work would also include using the change in phase to calculate and quantify the depth of the defect within the coating system, which was shown in Equation 5.4. Design of a probability of detection sample calibration system to measure the limitations of the method when applied to different materials is recommended in order to validate sensitivity of the thermal imaging process. These calibration samples are suggested to have multiple EDM notches with high volume of varying crack and pit sizes to establish a basis for all confidence curves of each crack, defect, and material system. Future work would also include an extension of the COMSOL simulation to better model the cooling period to estimate thermal responses while implementing phase analysis. Finally, using this novel system on curved geometries to understand the effect of angles of probing would provide valuable information for inspections of leading and trailing edges in aircraft systems and other complex geometries typical of aircraft parts.

APPENDIX A: DESIGN EVALUATION MATRIX

Figure A.1: Evaluation Matrix of Non-destructive Techniques for Corrosion detection under insulation

Block 1

Criteria	Importance Weight	Hyperspectral Imaging Rating	Weighted Rating	Terahertz Imaging Rating	Weighted Rating	Ultrasonic Guided Waves Rating	Weighted Rating	PEC Thermography* Rating	Weighted Rating	Pulsed Acoustic Laser Rating	Weighted Rating	Microwave Imaging Rating	Weighted Rating
Time of Scan	15.00%	2	0.3	13	1.95	3	0.45	2	0.3	5	0.75	13	1.95
Area of Scan	15.00%	2	0.3	13	1.95	3	0.45	3	0.45	8	1.2	13	1.95
Depth of Scan	20.00%	13	2.6	2	0.4	2	0.4	3	0.6	5	1	3	0.6
Maturity	10.00%	5	0.5	8	0.8	3	0.3	3	0.3	5	0.5	8	0.8
# of Sub-systems	10.00%	5	0.5	5	0.5	5	0.5	5	0.5	5	0.5	8	0.8
Size of Equipment	10.00%	3	0.3	13	1.3	3	0.3	3	0.3	5	0.5	5	0.5
Portability	10.00%	3	0.3	13	1.3	3	0.3	3	0.3	8	0.8	5	0.5
Cost	10.00%	3	0.3	13	1.3	8	0.8	3	0.3	8	0.8	13	1.3
Total	100.00%		5.1		9.5		3.5		3.05		6.05		8.4

Block 2

Criteria	Importance Weight	Radio Frequency Identification (RFID) Rating	Weighted Rating	Infrared Thermography Rating	Weighted Rating	Acoustic Emission Rating	Weighted Rating	Compton Back Scattering Rating	Weighted Rating	Electrochemical Cell Rating	Weighted Rating	Magnetic Flux Leakage* Rating	Weighted Rating
Time of Scan	15.00%	2	0.3	2	0.3	2	0.3	8	1.2	5	0.75	8	1.2
Area of Scan	15.00%	2	0.3	2	0.3	3	0.45	8	1.2	8	1.2	3	0.45
Depth of Scan	20.00%	2	0.4	2	0.4	3	0.6	1	0.2	3	0.6	5	1
Maturity	10.00%	8	0.8	3	0.3	3	0.3	8	0.8	3	0.3	5	0.5
# of Sub-systems	10.00%	3	0.3	3	0.3	3	0.3	5	0.5	5	0.5	5	0.5
Size of Equipment	10.00%	13	1.3	8	0.8	3	0.3	5	0.5	2	0.2	5	0.5
Portability	10.00%	5	0.5	8	0.8	8	0.8	8	0.8	2	0.2	3	0.3
Cost	10.00%	13	1.3	13	1.3	3	0.3	8	0.8	5	0.5	13	1.3
Total	100.00%		5.2		4.5		3.35		6		4.25		5.75

Block 3

Criteria	Importance Weight	Eddy Currents Rating	Weighted Rating	Pulsed Eddy Current Rating	Weighted Rating	Gradient Pulsed Eddy Current Rating	Weighted Rating	Pulse Modulated Eddy Current Rating	Weighted Rating	Microwave Waveguides OERW Rating	Weighted Rating	Phased Array Ultrasonic Rating	Weighted Rating
Time of Scan	15.00%	8	1.2	8	1.2	8	1.2	8	1.2	13	1.95	2	0.3
Area of Scan	15.00%	5	0.75	3	0.45	2	0.3	2	0.3	13	1.95	3	0.45
Depth of Scan	20.00%	5	1	3	0.6	2	0.4	5	1	2	0.4	2	0.4
Maturity	10.00%	2	0.2	3	0.3	3	0.3	3	0.3	3	0.3	5	0.5
# of Sub-systems	10.00%	5	0.5	5	0.5	5	0.5	3	0.3	5	0.5	5	0.5
Size of Equipment	10.00%	8	0.8	8	0.8	8	0.8	8	0.8	5	0.5	3	0.3
Portability	10.00%	5	0.5	5	0.5	5	0.5	5	0.5	8	0.8	3	0.3
Cost	10.00%	3	0.3	5	0.5	5	0.5	5	0.5	13	1.3	5	0.5
Total	100.00%		5.25		4.85		4.5		4.9		7.7		3.25

LIST OF REFERENCES

[1] Gustafsson, S., "Corrosion properties of aluminium alloys and surface treated alloys in tap water," *Sapa Technology*, 2011.

[2] Weissenrieder, J. and Leygraf, C., "In Situ Studies of Filiform Corrosion of Iron," *Journal of the Electrochemical Society*, Vol. 151, No. 3, 2004, pp. 165–171.

[3] Stavros, A. J. and Paxton, H. W., "Stress-corrosion cracking behavior of an 18 Pct Ni maraging steel," *Metallurgical Transactions*, Vol. 1, No. 11, 1970, pp. 3049–3055.

[4] Fischer, C. and Kakoulli, I., "Multispectral and hyperspectral imaging technologies in conservation: current research and potential applications," *Studies in Conservation*, Vol. 51, No. sup1, 2006, pp. 3–16.

[5] Anastasi, R. F., Madaras, E. I., Directorate, V. T., Evaluation, N., Branch, S., Evaluation, N., and Branch, S., "Terahertz Nde for Under Paint Corrosion," *32nd Annual Review of Progress in Quantitative Nondestructive Evaluation (AIP Conf. Proc. 820)*, Vol. 25, 2006, pp. 515–522.

[6] Sophian, A., Tian, G., and Fan, M., "Pulsed Eddy Current Non-destructive Testing and Evaluation: A Review," *Chinese Journal of Mechanical Engineering (English Edition)*, Vol. 30, No. 3, 2017, pp. 500–514.

[7] Zhang, H., He, Y., Gao, B., Tian, G. Y., Xu, L., and Wu, R., "Evaluation of Atmospheric Corrosion on Coated Steel Using K-Band Sweep Frequency Microwave Imaging," *IEEE Sensors Journal*, Vol. 16, No. 9, 2016, pp. 3025–3033.

[8] Nazir, M. H., Khan, Z. A., and Saeed, A., "A Novel Non-Destructive Sensing Technology for On-Site Corrosion Failure Evaluation of Coatings," *IEEE Access*, Vol. 6, 2017, pp. 1042–1054.

[9] Alamin, M., Tian, G., Andrews, A., and Jackson, P., "Corrosion detection using low-frequency RFID technology," *Insight-Non-Destructive Testing and Condition Monitoring*, Vol. 54, No. 2, 2012, pp. 72–75.

[10] He, Y., McLaughlin, S., Lo, J., Shi, C., Lenos, J., and Vincelli, A., "Radio frequency identification (RFID) based corrosion monitoring sensors Part 1–Component selection and testing," *Corrosion Engineering, Science and Technology*, Vol. 50, No. 1, 2015, pp. 63–71.

[11] Zhu, W., Rose, J. L., Barshinger, J. N., and Agarwala, V. S., "Ultrasonic guided wave NDT for hidden corrosion detection," *Research in Nondestructive Evaluation*, Vol. 10, No. 4, 1998, pp. 205–225.

[12] Jirarungsatian, C. and Prateepasen, A., "Pitting and uniform corrosion source recognition using acoustic emission parameters," *Corrosion Science*, Vol. 52, No. 1, 2010, pp. 187–197.

[13] Yang, R., He, Y., Zhang, H., and Huang, S., "Through coating imaging and nondestructive visualization evaluation of early marine corrosion using electromagnetic induction thermography," *Ocean Engineering*, Vol. 147, No. September 2017, 2018, pp. 277–288.

[14] Cheng, L. and Tian, G. Y., "Surface crack detection for carbon fiber reinforced plastic (CFRP) materials using pulsed eddy current thermography," *IEEE Sensors Journal*, Vol. 11, No. 12, 2011, pp. 3261–3268.

[15] Tian, G. Y., He, Y., Cheng, L., and Jackson, P., "Pulsed eddy current thermography for corrosion characterisation," *International Journal of Applied Electromagnetics and Mechanics*, Vol. 39, No. 1-4, 2012, pp. 269–276.

[16] Huang, X., Yin, C., Dadras, S., Cheng, Y., and Bai, L., "Adaptive rapid defect identification in ECPT based on K-means and automatic segmentation algorithm," *Journal of Ambient Intelligence and Humanized Computing*, 2018, pp. 1–18.

[17] Gao, B., Bai, L., Woo, W. L., Tian, G. Y., and Cheng, Y., "Automatic defect identification of eddy current pulsed thermography using single channel blind source separation," *IEEE Transactions on Instrumentation and Measurement*, Vol. 63, No. 4, 2014, pp. 913–922.

[18] Shi, Z., Xu, X., Ma, J., Zhen, D., and Zhang, H., "Quantitative detection of cracks in steel using eddy current pulsed thermography," *Sensors (Switzerland)*, Vol. 18, No. 4, 2018.

[19] Hertzberg, E. F., Guo, S., Stroh, R. F., Chan, T. K., Morris, A., and Stevenson, A., "Estimated Impact of Corrosion on Cost and Availability of DoD Weapon Systems: FY2018 Update," , No. March, 2018.

[20] Pozar, D. M., "A modern course in microwave engineering," *IEEE Transactions on Education*, Vol. 33, No. 1, 1990, pp. 129–134.

[21] Oldfield, J. W., "Electrochemical theory of galvanic corrosion," *Galvanic Corrosion*, ASTM International, 1988.

[22] TOMASHOV, N. D., "Development of the Electrochemical Theory of Metallic Corrosion," 1964.

[23] Newman, R., "Pitting corrosion of metals," *The Electrochemical Society Interface*, Vol. 19, No. 1, 2010, pp. 33–38.

[24] Liao, M., Bellinger, N., and Komorowski, J., "Modeling the effects of prior exfoliation corrosion on fatigue life of aircraft wing skins," *International Journal of Fatigue*, Vol. 25, No. 9-11, 2003, pp. 1059–1067.

[25] Liao, M., Renaud, G., and Bellinger, N., "Fatigue modeling for aircraft structures containing natural exfoliation corrosion," *International Journal of Fatigue*, Vol. 29, No. 4, 2007, pp. 677–686.

[26] R., D., "Corrosion Control for Aircraft AC 43-4B," Tech. rep., FAA, 2018.

[27] RAO, A. C., VASU, V., GOVINDARAJU, M., and SRINADH, K. V., "Stress corrosion cracking behaviour of 7xxx aluminum alloys: A literature review," *Transactions of Nonferrous Metals Society of China (English Edition)*, Vol. 26, No. 6, 2016, pp. 1447–1471.

[28] Sussex, W., "Corrosion and Inspection of General Aviation Aircraft CAP 1570," .

[29] Shaw, B. A. and Kelly, R. G., "What is corrosion?" *Electrochemical Society Interface*, Vol. 15, No. 1, 2006, pp. 24–26.

[30] Frankel, G. S., "Active Protective Coatings," *Active Protective Coatings*, Vol. 233, 2016, pp. 17–32.

[31] Scully, J. C., *The Fundementals of Corrosion*, UK, 2nd ed., 1975.

[32] others Schweitzer, P. A., *Fundamentals of Corrosion: mechanisms, causes, and preventative methods*, CRC press, 2009.

[33] Rosenfeld, I. and Marshakov, I., "Mechanism of crevice corrosion," *Corrosion*, Vol. 20, No. 4, 1964, pp. 115t–125t.

[34] Rashidi, N., Alavi-soltani, S., and Asmatulu, R., "Crevice Corrosion Theory, Mechanisms and Prevention Methods," *Proceedings of the 3rd Annual GRASP Symposium*, 2007, pp. 215–216.

[35] Slabaugh, W. H. and Grotheer, M., "Mechanism of Filiform Corrosion," *Industrial & Engineering Chemistry*, Vol. 46, No. 5, 1954, pp. 1014–1016.

[36] DuQuesnay, D. L., Underhill, P. R., and Britt, H. J., "Fatigue crack growth from corrosion damage in 7075-T6511 aluminium alloy under aircraft loading," *International Journal of Fatigue*, Vol. 25, No. 5, 2003, pp. 371–377.

[37] Alonzo, M., Bookhagen, B., and Roberts, D. A., "Urban tree species mapping using hyperspectral and lidar data fusion," *Remote Sensing of Environment*, Vol. 148, 2014, pp. 70–83.

[38] Bonifazi, G., Capobianco, G., and Serranti, S., "Asbestos containing materials detection and classification by the use of hyperspectral imaging," *Journal of hazardous materials*, Vol. 344, 2018, pp. 981–993.

[39] Mahesh, S., Jayas, D., Paliwal, J., and White, N., "Hyperspectral imaging to classify and monitor quality of agricultural materials," *Journal of Stored Products Research*, Vol. 61, 2015, pp. 17–26.

[40] Manley, M., "Near-infrared spectroscopy and hyperspectral imaging: non-destructive analysis of biological materials," *Chemical Society Reviews*, Vol. 43, No. 24, 2014, pp. 8200–8214.

[41] Sakagami, T. and Kubo, S., "Applications of pulse heating thermography and lock-in thermography to quantitative nondestructive evaluations," *Infrared Physics and Technology*, Vol. 43, No. 3-5, 2002, pp. 211–218.

[42] Chou, S., Stutzman, P., Provenzano, V., McMichael, R., Surek, J., Wang, S., Plusquellic, D., and Garboczi, E., "Using Terahertz Waves to Identify the Presence of Goethite via Antiferromagnetic Resonance," *Applied Magnetic Resonance*, Vol. 48, No. 6, 2017, pp. 559–569.

[43] Fan, S., Qi, F., Notake, T., Nawata, K., Takida, Y., Matsukawa, T., and Minamide, H., "Diffraction-limited real-time terahertz imaging by optical frequency up-conversion in a DAST crystal," *Optics express*, Vol. 23, No. 6, 2015, pp. 7611–7618.

[44] Sophian, A., Tian, G. Y., Taylor, D., and Rudlin, J., "A feature extraction technique based on principal component analysis for pulsed Eddy current NDT," *NDT and E International*, Vol. 36, No. 1, 2003, pp. 37–41.

[45] Sodano, H. A., "Development of an automated eddy current structural health monitoring technique with an extended sensing region for corrosion detection," *Structural Health Monitoring*, Vol. 6, No. 2, 2007, pp. 111–119.

[46] He, Y., Luo, F., and Pan, M., "Defect characterisation based on pulsed eddy current imaging technique," *Sensors and Actuators A: Physical*, Vol. 164, No. 1-2, 2010, pp. 1–7.

[47] Chen, X. and Lei, Y., "Electrical conductivity measurement of ferromagnetic metallic materials using pulsed eddy current method," *Ndt & E International*, Vol. 75, 2015, pp. 33–38.

[48] Li, J., Wu, X., Zhang, Q., and Sun, P., "Pulsed eddy current testing of ferromagnetic specimen based on variable pulse width excitation," *NDT & E International*, Vol. 69, 2015, pp. 28–34.

[49] Goda, T., Haga, Y., Tomioka, T., Sakai, K., Kiwa, T., and Tsukada, K., "Characterizing of Corrosion Backside of Steel Plates Using Extremely Low-Frequency Eddy Current Testing with Multiple-Frequency Magnetic-Field Exposure," *22nd International Workshop on Electromagnetic Nondestructive Evaluation, ENDE 2017*, IOS Press, 2018, pp. 130–135.

[50] Venkataraman, B. and Raj, B., "Performance parameters for thermal imaging systems," *Insight-Non-Destructive Testing and Condition Monitoring*, Vol. 45, No. 8, 2003, pp. 531–535.

[51] Clark, M., McCann, D., and Forde, M., "Application of infrared thermography to the nondestructive testing of concrete and masonry bridges," *NDT & E International*, Vol. 36, 06 2003, pp. 265–275.

[52] Maldague, X. and Marinetti, S., "Pulse phase infrared thermography," *Journal of Applied Physics*, Vol. 79, No. 5, 1996, pp. 2694–2698.

[53] Maldague, X. P. V., "Introduction to NDT by active infrared thermography," *Materials Evaluation*, Vol. 60, No. 9, 2002, pp. 1060–1073.

[54] Vavilov, V., Grinzato, E., Bison, P. G., Marinetti, S., and Bales, M. J., "Surface transient temperature inversion for hidden corrosion characterisation: Theory and applications," *International Journal of Heat and Mass Transfer*, Vol. 39, No. 2, 1996, pp. 355–371.

[55] Grinzato, E., Vavilov, V., Bison, P. G., and Marinetti, S., "Hidden corrosion detection in thick metallic components by transient IR thermography," *Infrared Physics and Technology*, Vol. 49, No. 3 SPEC. ISS., 2007, pp. 234–238.

[56] Bagavathiappan, S., Lahiri, B. B., Saravanan, T., Philip, J., and Jayakumar, T., "Infrared thermography for condition monitoring - A review," *Infrared Physics and Technology*, Vol. 60, 2013, pp. 35–55.

[57] Haneef, T., Lahiri, B. B., Bagavathiappan, S., Mukhopadhyay, C. K., Philip, J., Rao, B. P. C., and Jayakumar, T., "Study of the tensile behavior of AISI type 316 stainless steel using acoustic emission and infrared thermography techniques," *Journal of Materials Research and Technology*, Vol. 4, No. 3, 2015, pp. 241–253.

[58] He, Y., Tian, G., Cheng, L., Zhang, H., and Jackson, P., "Parameters influence in steel corrosion evaluation using PEC thermography," *Proceedings of 2011 17th International Conference on Automation and Computing, ICAC 2011*, , No. September, 2011, pp. 255–260.

[59] Hughes, D., Wang, N., Case, T., Donnell, K., Zoughi, R., Austin, R., and Novack, M., "Microwave nondestructive detection of corrosion under thin paint and primer in aluminum

panels," *Subsurface Sensing Technologies and Applications*, Vol. 2, No. 4, 2001, pp. 435–471.

[60] Buyukozturk, O., Park, J., and Au, C., "Non-destructive evaluation of FRP-confined concrete using microwaves," *Proc. Int. Symp. Non-Destructive Testing in Civil Engineering, Berlin*, 2003, pp. 16–19.

[61] Zoughi, R. and Kharkovsky, S., "Microwave and millimetre wave sensors for crack detection," *Fatigue & Fracture of Engineering Materials & Structures*, Vol. 31, No. 8, 2008, pp. 695–713.

[62] Ramzi, M. R., Abou-Khousa, M., and Prayudi, I., "Near-field microwave imaging using open-ended circular waveguide probes," *IEEE sensors journal*, Vol. 17, No. 8, 2017, pp. 2359–2366.

[63] Jamali, S. S., Zhao, Y., Gao, Z., Li, H., and Hee, A. C., "In situ evaluation of corrosion damage using non-destructive electrochemical measurements—A case study," *Journal of Industrial and Engineering Chemistry*, Vol. 43, 2016, pp. 36–43.

[64] Fuse, N., Naganuma, A., Fukuchi, T., Hori, Y., Mizuno, M., and Fukunaga, K., "Underfilm corrosion of transmission tower cross-arms service-used in a Pacific Coast Area," *Corrosion*, Vol. 71, No. 11, 2015, pp. 1387–1397.

[65] Terry, M. T., Edgemon, G. L., Mickalonis, J. I., and Mizia, R. E., "Development and deployment of advanced corrosion monitoring systems for high-level waste tanks," Tech. rep., Los Alamos National Laboratory PO Box 1663, Los Alamos, NM (US); HiLine . . . , 2002.

[66] Parthiban, T., Ravi, R., and Parthiban, G. T., "Potential monitoring system for corrosion of steel in concrete," *Advances in Engineering Software*, Vol. 37, No. 6, 2006, pp. 375–381.

[67] Mueller, W. D., "Electrochemical techniques for assessment of corrosion behaviour of Mg and Mg-alloys," *BioNanoMaterials*, Vol. 16, No. 1, 2015, pp. 31–39.

[68] Zhang, H., Yang, R., He, Y., Tian, G. Y., Xu, L., and Wu, R., "Identification and characterisation of steel corrosion using passive high frequency RFID sensors," *Measurement*, Vol. 92, 2016, pp. 421–427.

[69] Sharma, S. and Mukherjee, A., "Nondestructive evaluation of corrosion in varying environments using guided waves," *Research in Nondestructive Evaluation*, Vol. 24, No. 2, 2013, pp. 63–88.

[70] Lozev, M. G., Smith, R. W., and Grimmett, B. B., "OMAE2003-37350," 2017, pp. 1–12.

[71] Fregonese, M., Idrissi, H., Mazille, H., Renaud, L., and Cetre, Y., "Initiation and propagation steps in pitting corrosion of austenitic stainless steels: monitoring by acoustic emission," *Corrosion science*, Vol. 43, No. 4, 2001, pp. 627–641.

[72] Zou, X., Schmitt, T., Perloff, D., Wu, N., Yu, T.-Y., and Wang, X., "Nondestructive corrosion detection using fiber optic photoacoustic ultrasound generator," *Measurement*, Vol. 62, 2015, pp. 74–80.

[73] Wong, Y., Thomas, R., and Hawkins, G., "Surface and subsurface structure of solids by laser photoacoustic spectroscopy," *Applied Physics Letters*, Vol. 32, No. 9, 1978, pp. 538–539.

[74] Chen, X., Cheng, L., Guo, D., Kostov, Y., and Choa, F.-S., "Quantum cascade laser based standoff photoacoustic chemical detection," *Optics express*, Vol. 19, No. 21, 2011, pp. 20251–20257.

[75] He, Y., Tian, G., Zhang, H., Alamin, M., Simm, A., and Jackson, P., "Steel corrosion characterization using pulsed eddy current systems," *IEEE Sensors Journal*, Vol. 12, No. 6, 2012, pp. 2113–2120.

[76] He, Y., Pan, M., and Luo, F., "Defect characterisation based on heat diffusion using induction thermography testing," *Review of Scientific Instruments*, Vol. 83, No. 10, 2012.

[77] Goda, T., Haga, Y., Tomioka, T., Sakai, K., Kiwa, T., and Tsukada, K., "Characterizing of corrosion backside of steel plates using extremely low-frequency eddy current testing with multiple-frequency magnetic-field exposure," *Studies in Applied Electromagnetics and Mechanics*, Vol. 43, No. Xxi, 2018, pp. 130–135.

[78] Cheng, L. and Tian, G. Y., "Transient thermal behavior of eddy-current pulsed thermography for nondestructive evaluation of composites," *IEEE Transactions on Instrumentation and Measurement*, Vol. 62, No. 5, 2013, pp. 1215–1222.

[79] Cheng, L., Gao, B., Tian, G. Y., Woo, W. L., and Berthiau, G., "Impact damage detection and identification using eddy current pulsed thermography through integration of PCA and ICA," *IEEE Sensors Journal*, Vol. 14, No. 5, 2014, pp. 1655–1663.

[80] Yang, S., Tian, G. Y., Abidin, I. Z., and Wilson, J., "Simulation of edge cracks using pulsed eddy current stimulated thermography," *Journal of Dynamic Systems, Measurement, and Control*, Vol. 133, No. 1, 2011.

[81] He, Y., Pan, M., Tian, G., Chen, D., Tang, Y., and Zhang, H., "Eddy current pulsed phase thermography for subsurface defect quantitatively evaluation," *Applied Physics Letters*, Vol. 103, No. 14, 2013.

[82] Zhou, X., Xue, Y., Tian, G., and Liu, Z., "Thermal Analysis of Solder Joint Based on Eddy Current Pulsed Thermography," *IEEE Transactions on Components, Packaging and Manufacturing Technology*, Vol. 7, No. 7, 2017, pp. 1111–1118.

[83] Rudnev, V., Loveless, D., and Cook, R. L., *Handbook of induction heating*, CRC press, 2017.

[84] Davies, J., *Conduction and induction heating*, No. 11, IET, 1990.

[85] Semiatin, S., *Elements of induction heating: design, control, and applications*, ASM International, 1988.

[86] Benci, V. and Fortunato, D., "An eigenvalue problem for the Schrödinger-Maxwell equations," *Topological Methods in Nonlinear Analysis*, Vol. 11, No. 2, 1998, pp. 283–293.

[87] Barton, J. P. and Alexander, D. R., "Fifth-order corrected electromagnetic field components for a fundamental Gaussian beam," *Journal of Applied Physics*, Vol. 66, No. 7, 1989, pp. 2800–2802.

[88] Hiptmair, R., "Finite elements in computational electromagnetism," *Acta Numerica*, Vol. 11, 2002, pp. 237–339.

[89] Liu, F., Yang, S., Leng, C., and Su, Z., "Simulation on quantitative analysis of crack inspection by using eddy current stimulated thermography," *FENDT 2013 - Proceedings of 2013 Far East Forum on Nondestructive Evaluation/Testing: New Technology and Application*, 2013, pp. 59–64.

[90] Wilson, J., Tian, G. Y., Abidin, I. Z., Yang, S., and Almond, D., "Modelling and evaluation of eddy current stimulated thermography," *Nondestructive Testing and Evaluation*, Vol. 25, No. 3, 2010, pp. 205–218.

[91] Howell, J. R., Menguc, M. P., and Siegel, R., *Thermal radiation heat transfer*, CRC press, 2015.

[92] Vollmer, M. and Möllmann, K.-P., *Infrared thermal imaging: fundamentals, research and applications*, John Wiley & Sons, 2017.

[93] Kylili, A., Fokaides, P. A., Christou, P., and Kalogirou, S. A., "Infrared thermography (IRT) applications for building diagnostics: A review," *Applied Energy*, Vol. 134, 2014, pp. 531–549.

[94] Fokaides, P. A. and Kalogirou, S. A., "Application of infrared thermography for the determination of the overall heat transfer coefficient (U-Value) in building envelopes," *Applied energy*, Vol. 88, No. 12, 2011, pp. 4358–4365.

[95] Tsopelas, N. and Siakavellas, N. J., "Electromagnetic-thermal NDT in thin conducting plates," *NDT and E International*, Vol. 39, No. 5, 2006, pp. 391–399.

[96] Tsopelas, N. and Siakavellas, N. J., "Performance of circular and square coils in electromagnetic-thermal non-destructive inspection," *NDT and E International*, Vol. 40, No. 1, 2007, pp. 12–28.

[97] Tsopelas, N. and Siakavellas, N. J., "The effect of the angle of inclination of the exciting coil in electromagnetic-thermal non-destructive inspection," *International Journal of Materials and Product Technology*, Vol. 41, No. 1-4, 2011, pp. 162–177.

[98] Tian, G. Y., Wilson, J., Cheng, L., Almond, D. P., Kostson, E., and Weekes, B., "Pulsed eddy current thermography and applications," *Lecture Notes in Electrical Engineering*, Vol. 96, 2011, pp. 205–231.

[99] Tian, G. Y., Sophian, A., Taylor, D., and Rudlin, J., "Multiple sensors on pulsed eddy-current detection for 3-D subsurface crack assessment," *IEEE Sensors Journal*, Vol. 5, No. 1, 2005, pp. 90–96.

[100] Maldague, X. and Marinetti, S., "Pulse phase infrared thermography," *Journal of Applied Physics*, Vol. 79, No. 5, 1996, pp. 2694–2698.

[101] Maldague, X., Galmiche, F., and Ziadi, A., "Advances in pulsed phase thermography," *Infrared physics & technology*, Vol. 43, No. 3-5, 2002, pp. 175–181.